Super-Gaussian transport theory and the field-generating thermal instability in laser–plasmas

2013 New J. Phys. 15 025017

(http://iopscience.iop.org/1367-2630/15/2/025017)

New Journal of Physics
The open access journal for physics

Super-Gaussian transport theory and the field-generating thermal instability in laser–plasmas

J J Bissell[1,2,5], C P Ridgers[2,3] and R J Kingham[2,4]

[1] Department of Mathematical Sciences, University of Durham, Durham DH1 3LE, UK
[2] Blackett Laboratory, Imperial College London, London SW7 2BZ, UK
[3] Clarendon Laboratory, University of Oxford, Oxford OX1 3PU, UK
[4] Central Laser Facility, Rutherford-Appleton Laboratory, Oxon OX11 0QX, UK
E-mail: john.bissell@durham.ac.uk

New Journal of Physics **15** (2013) 025017 (32pp)
Received 31 August 2012
Published 8 February 2013
Online at http://www.njp.org/
doi:10.1088/1367-2630/15/2/025017

Abstract. Inverse bremsstrahlung (IB) heating is known to distort the electron distribution function in laser–plasmas from a Gaussian towards a super-Gaussian, thereby modifying the equations of classical transport theory (Ridgers *et al* 2008 *Phys. Plasmas* **15** 092311). Here we explore these modified equations, demonstrating that super-Gaussian effects both suppress traditional transport processes, while simultaneously introducing new effects, such as isothermal (*anomalous Nernst*) magnetic field advection *up* gradients in the electron number density n_e, which we associate with a novel heat-flow $\mathbf{q}_n \propto \nabla n_e$. Suppression of classical phenomena is shown to be most pronounced in the limit of low Hall-parameter χ, in which case the Nernst effect is reduced by a factor of five, the $\nabla T_e \times \nabla n_e$ field generation mechanism by $\sim$30% (where T_e is the electron temperature), and the diffusive and Righi–Leduc heat-flows by $\sim$80 and $\sim$90% respectively. The new isothermal field advection phenomenon and associated density-gradient driven heat-flux $\mathbf{q}_n$ are checked against kinetic simulation using the Vlasov–Fokker–Planck code IMPACT, and interpreted in relation to the underlying super-Gaussian distribution through simplified kinetic

[5] Author to whom any correspondence should be addressed.

analysis. Given such strong inhibition of transport at low χ, we consider the impact of IB on the seeding and evolution of magnetic fields (in otherwise unmagnetized conditions) by examining the well-known field-generating thermal instability in the light of super-Gaussian transport theory (Tidman and Shanny 1974 *Phys. Fluids* **12** 1207). Estimates based on conditions in an inertial confinement fusion (ICF) hohlraum suggest that super-Gaussian effects can reduce the growth-rate of the instability by $\gtrsim 80\%$. This result may be important for ICF experiments, since by increasing the strength of IB heating it would appear possible to inhibit the spontaneous generation of large magnetic fields.

Contents

1. Introduction

Accurate prediction of transport phenomena, such as the flow heat and advection of magnetic fields, is essential to the success of long-pulse (100 ps–10 ns) laser–plasma experiments, including those at the National Ignition Facility [1–10]. Typically, electron transport is modelled using magnetohydrodynamic fluid equations closed with Braginskii's classical transport theory, under the assumption that—at time t and spatial $\mathbf{r}$ and velocity $\mathbf{v}$ phase-space coordinates—the isotropic part $f_0(\mathbf{r}, |\mathbf{v}|, t)$ of the electron distribution function $f(\mathbf{r}, \mathbf{v}, t)$ is approximately Gaussian: specifically, $f_0 \propto \exp(-[v/v_T]^2)$, where $v = |\mathbf{v}|$, $v_T = (2T_e/m_e)^{1/2}$ is the thermal velocity, T_e is the electron temperature in energy units, and m_e is the electron mass [1, 11–13]. However, for laser intensities in the range 10^{14}–10^{16} $W\,cm^{-2}$ (characteristic of long-pulse experiments), heating is dominated by inverse bremsstrahlung (IB), a mechanism which distorts f_0 away from a Gaussian by preferentially transmitting energy to slower, more collisional

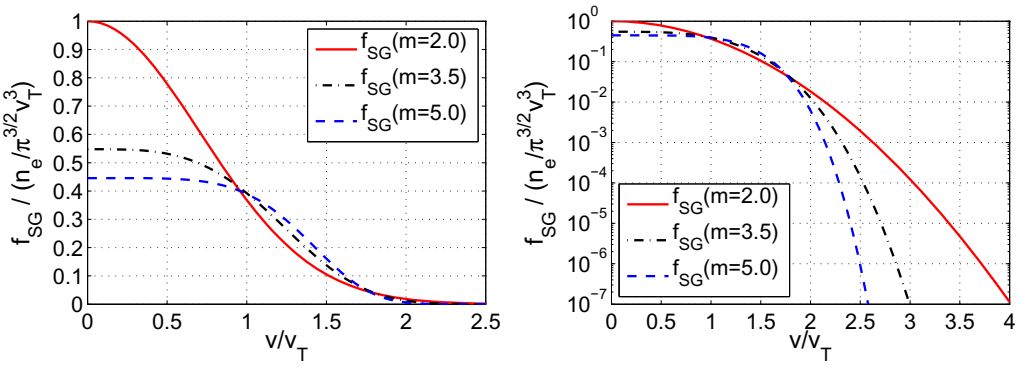

Figure 1. The super-Gaussian distribution $f_{\mathrm{SG}} \propto \exp(-[v/\alpha_{\mathrm{e}} v_{\mathrm{T}}]^m)$ plotted for a range of m and normalized to $n_{\mathrm{e}}/(\pi^{1/2} v_{\mathrm{T}})^3$. Notice the reduced number of high energy (fast) electrons in the $v > 2v_{\mathrm{T}}$ tail of the super-Gaussian distributions ($m > 2$) when compared to the usual Gaussian form ($m = 2$).

electrons. Indeed, under these conditions the isotropic part of the distribution function is better described by a super-Gaussian f_{SG}, i.e.

$$f_0 \to f_{\mathrm{SG}}(v) = C(m)\frac{n_{\mathrm{e}}}{v_{\mathrm{T}}^3}\exp\left[-\left(\frac{v}{\alpha_{\mathrm{e}} v_{\mathrm{T}}}\right)^m\right], \quad \text{with} \quad m \in [2,5], \tag{1}$$

$$\alpha_{\mathrm{e}}^2 = \frac{3\tilde{\Gamma}(3/m)}{2\tilde{\Gamma}(5/m)} \quad \text{and} \quad C = \frac{m}{4\pi\alpha_{\mathrm{e}}^3\tilde{\Gamma}(3/m)}, \quad \text{here} \quad \tilde{\Gamma}(x) = \int_0^\infty s^{x-1}\,\mathrm{e}^{-s}\,\mathrm{d}s$$

is the gamma function for $x \in \mathbb{R}^+$, while $\alpha_{\mathrm{e}}(m)$ and $C(m)$ ensure that f_{SG} is correctly normalized to yield the requisite number density n_{e} and energy density $U = \frac{3}{2}n_{\mathrm{e}}T_{\mathrm{e}}$ [14–17]. Notice that the range of super-Gaussian power $m \in [2, 5]$ yields the usual Gaussian distribution if $m = 2$, and tends to a Langdon distribution ($m = 5$) for very intense irradiation (see figure 1). For n_{e} less than approximately three-quarters critical density n_{c}, the super-Gaussian power m can be calculated from the ion atomic number Z by employing the formula of Matte *et al* [17]:

$$m = 2 + \frac{3}{1 + 1.66/\alpha_M^{0.724}}, \quad \text{where } \alpha_M = Z\frac{v_{\mathrm{osc.}}^2}{v_{\mathrm{T}}^2} \tag{2}$$

and the electron quiver velocity $v_{\mathrm{osc.}}$ may be estimated using the expression

$$\frac{v_{\mathrm{osc.}}^2}{v_{\mathrm{T}}^2} \approx \left(\frac{0.093}{\alpha_{\mathrm{l}}}\right)\left(\frac{I_{\mathrm{l}}\lambda_{\mathrm{l}}^2}{10^{15}\,\mathrm{W\,cm^{-2}}\,\mu\mathrm{m}^2}\right)\left(\frac{T_{\mathrm{e}}}{\mathrm{keV}}\right)^{-1}, \tag{3}$$

provided the laser intensity I_{l} and wavelength λ_{l} are measured in $\mathrm{W\,cm^{-2}}$ and $\mu\mathrm{m}^2$ respectively, and T_{e} is measured in keV (the dimensionless number α_{l} takes the value $\alpha_{\mathrm{l}} = 1/2$ if the light is linearly polarized and $\alpha_{\mathrm{l}} = 1$ if it is circularly polarized) [18, 19].

Since distortion to the distribution function invalidates classical transport, Ridgers *et al* developed a revised transport theory based on super-Gaussian distribution functions, thereby providing a solution to the problem of modelling IB effects in fluid codes without recourse to computationally expensive kinetic calculations [14, 15]. In this new *super-Gaussian transport theory*, the modified classical expressions for both the electric field **E** (Ohm's law) and the total

Table 1. Example values of the super-Gaussian transport coefficients for $\chi = 0$, showing their variation with increasing m (as calculated from the expressions of Ridgers *et al* [14] discussed in appendix C). The subscript '$\|$' notation is described in section 2.

m	$\alpha^c_\|$	$\beta^c_\|$	$\gamma^c_\|$	$\kappa^c_\|$	$\psi^c_\|$	$\phi^c_\|$
2.0	0.295	1.500	1.000	13.58	1.500	−0.000
3.0	0.310	1.250	0.833	7.171	0.833	−0.712
4.0	0.318	1.144	0.763	5.184	0.551	−0.851
5.0	0.323	1.087	0.725	4.269	0.398	−0.894

heat-flow $\mathbf{q}$ (heat-flow equation) become

$$en_e(\mathbf{E}+\mathbf{C}\times\mathbf{B}) = -\underline{\underline{\gamma}}^c\cdot\nabla P_e + \mathbf{j}\times\mathbf{B} + \frac{m_e}{e\tau_B}\underline{\underline{\alpha}}^c\cdot\mathbf{j} - n_e\underline{\underline{\beta}}^c\cdot\nabla T_e \tag{4}$$

$$\text{and}\quad \mathbf{q} = -\frac{n_e\tau_B T_e}{m_e}\underline{\underline{\kappa}}^c\cdot\nabla T_e - \underline{\underline{\psi}}'\cdot\mathbf{j}\frac{T_e}{e} - \frac{\tau_B T_e}{m_e}\underline{\underline{\phi}}^c\cdot\nabla P_e, \tag{5}$$

where e is the elementary electronic charge, $P_e = n_e T_e$ is the isotropic pressure, $\mathbf{j}$ is the current, $\mathbf{C}$ is the bulk flow velocity, $\mathbf{B}$ is the magnetic field flux-density and $\tau_B = c_B\tau_T$ is the Braginkii collision time, which is proportional to the thermal collision time τ_T by the factor $c_B = 3\sqrt{\pi}/4$; with ion number density $n_i \approx n_e/Z$, permittivity of free space ϵ_0, and Coulomb logarithm $\log\Lambda_{ei} \approx 8$, τ_T is itself given by $\tau_T = (4\pi v_T^3)/(n_i[Ze^2/\epsilon_0 m_e]^2\log\Lambda_{ei})$. Ridgers used the Lorentz approximation, so that with $\underline{\underline{\mathbf{I}}}$ as the identity tensor, the transport coefficients $\underline{\underline{\alpha}}^c$, $\underline{\underline{\beta}}^c$, $\underline{\underline{\kappa}}^c$, $\underline{\underline{\psi}}^c = \underline{\underline{\psi}}' - [5/2]\underline{\underline{\mathbf{I}}}$, $\underline{\underline{\gamma}}^c$ and $\underline{\underline{\phi}}^c$ are dimensionless functions of both m and the Hall parameter $\chi = \omega_L\tau_B$ only, where $\omega_L = (e|\mathbf{B}|/m_e)$ is the electron Larmor frequency [14][6]. Naturally, the super-Gaussian theory reduces to the classical theory when $m = 2$, in which case $\underline{\underline{\beta}}^c = \underline{\underline{\psi}}^c$, $\underline{\underline{\gamma}}^c = \underline{\underline{\mathbf{I}}}$ and $\underline{\underline{\phi}}^c = \underline{\underline{0}}$. The resistivity $\underline{\underline{\alpha}}^c$, conductivity $\underline{\underline{\kappa}}^c$, and thermoelectric tensors $\underline{\underline{\beta}}^c$ and $\underline{\underline{\psi}}^c$ may thus be termed 'old' coefficients, whose values are modified depending on the super-Gaussian power m, while $\underline{\underline{\gamma}}^c$ and $\underline{\underline{\phi}}^c$ are 'new' coefficients describing IB effects. Further details of how these coefficients are calculated are given in appendix C.

However, while Ridgers *et al* [14] demonstrated the applicability of the super-Gaussian transport theory to experiment [5, 9], and noted changes to the 'old' coefficients (see table 1), they did not fully consider the implications of the new terms. In an attempt to redress this omission, therefore, the first part of this paper (section 2) explores some of the ways that the super-Gaussian coefficients $\underline{\underline{\phi}}^c$ and $\underline{\underline{\gamma}}^c$ might be expected to influence transport in magnetized plasmas. Classical transport phenomena, though often key to understanding laser–plasma interactions, are themselves not universally known, and in part this section necessarily represents a review of some important phenomena. We show that the addition of 'new' coefficients has two principal consequences: firstly, the suppression of conventional transport; and secondly, the introduction of new ∇n_e driven effects which persist when the

[6] In the heat-flow equation (equation (5)) $\underline{\underline{\psi}}'$ accounts for the relationship $\mathbf{q} = \mathbf{q}'_e - (5T_e)/(2e)\mathbf{j}$ between the total heat-flow $\mathbf{q}$ and the approximate intrinsic heat-flow $\mathbf{q}'_e$, so that $\underline{\underline{\psi}}' = \underline{\underline{\psi}}^c + (5/2)\underline{\underline{\mathbf{I}}}$ [18, 20].

temperature is uniform, specifically isothermal $\mathbf{q}_n \propto \nabla n_e$ heat-flow, and associated *anomalous Nernst* advection of the magnetic field. In particular, we demonstrate that transport is strongly affected by IB in the limit of low χ, suggesting that the super-Gaussian theory may be most relevant to the seeding and evolution of magnetic fields in otherwise un-magnetized conditions. Since part of our motivation is to relate the new phenomena to the underlying super-Gaussian distribution function, we supplement our discussion with both kinetic analysis and numerical simulation (using our Vlasov–Fokker–Planck (VFP) code IMPACT [23]) in section 3.

Knowledge of the dual consequences of the extended theory leads naturally to questions about the combination of effects, especially in contexts of pronounced feedback when χ is small. Accordingly, the second half of our discussion (section 4) is devoted to assessing how super-Gaussian phenomena impact on the well known field-generating thermal instability [24–28]. In fact, this half affords us the opportunity to further more general understanding of the instability, both in terms of quantitative prediction (by providing peak growth-rate expressions currently absent from the literature) and physical interpretation.

It should be recognized that the possibility of isothermal, density-gradient driven heat-flow $\mathbf{q}_n \propto \nabla n_e$ has previously been considered by Zhu and Gu [21] and Huo *et al* [22]; however, these authors restricted their attentions to unmagnetized conditions, and employed mainly analytical approaches. Here we extend understanding of the novel $\mathbf{q}_n$ phenomenon to magnetized plasmas, showing for the first time how it can lead to advection of magnetic fields as *anomalous Nernst* (see sections 2.2.3 and 3), and interpret its emergence physically (see section 3.3). Indeed, our numerical calculations (section 3) complement both the present analytical work and those of earlier studies [21, 22], since we: (i) verify dynamics arising from the super-Gaussian transport equations (4) and (5) in a 'first principles' fashion; and (ii) demonstrate their robustness given f_0 deviations from the exact super-Gaussian form f_{SG} due to collisional relaxation ($m \to 2$) and non-locality.

2. Super-Gaussian modifications to classical transport theory

In the following two subsections we describe new magnetized transport effects arising from the super-Gaussian coefficients $\underline{\underline{\phi}}^c$ and $\underline{\underline{\gamma}}^c$, and in doing so necessarily review some traditional phenomena. Before proceeding, however, note that in magnetized plasmas the **B**-field provides a unique direction of reference, and throughout our discussion it shall prove convenient to split transport into components parallel and perpendicular to field lines. In particular, if we consider a field unit vector $\mathbf{b} = \mathbf{B}/|\mathbf{B}|$ and a vector $\mathbf{s}$ in the direction of the driving force behind the transport (e.g. $\mathbf{s} = \nabla T_e$ for the thermal conductivity $\underline{\underline{\kappa}}^c$), then for a general transport coefficient $\underline{\underline{\eta}}$ we can form an orthogonal basis characterized by three functions $\eta_\perp(\chi, m)$, $\eta_\wedge(\chi, m)$ and $\underline{\underline{\eta}}_\parallel(m) = \eta_\perp(0, m)$, such that $\underline{\underline{\eta}} \cdot \mathbf{s} = \eta_\parallel \mathbf{b}(\mathbf{b}\cdot\mathbf{s}) + \eta_\perp \mathbf{b} \times (\mathbf{s} \times \mathbf{b}) + \eta_\wedge \mathbf{b} \times \mathbf{s}$ (see figure 2), where in the case of the resistivity $\underline{\underline{\alpha}}^c$ convention dictates that the final term has opposite polarity (i.e. $\mathbf{s} \to \mathbf{j}$, $\eta_\wedge \to -\eta_\wedge$ and $\eta \to \alpha$). However, for added ease when illustrating phenomena, we shall assume a geometry in which gradients and fluxes are taken to be perpendicular to the magnetic field **B**, that is, for scalar quantities ϕ and vector quantities **A** we have $\mathbf{B}\cdot\nabla\phi = \mathbf{B}\cdot\mathbf{A} = 0$. In this case, the coefficient components may be simplified to

$$\underline{\underline{\eta}} \cdot \mathbf{s} = \eta_\perp \mathbf{s} + \eta_\wedge \mathbf{b} \times \mathbf{s}. \tag{6}$$

Note that when $\chi = 0$ one may write $\underline{\underline{\eta}} = \eta_\parallel \underline{\underline{\mathbf{I}}}$, hence the notation in table 1.

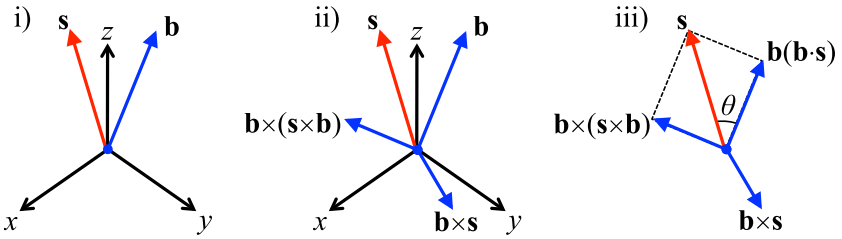

Figure 2. Three diagrams narrating the construction of the general orthogonal transport basis $\{\mathbf{b}(\mathbf{b}\cdot\mathbf{s}),\ \mathbf{b}\times(\mathbf{s}\times\mathbf{b}), \mathbf{b}\times\mathbf{s}\}$ as follows: (i) firstly, the driving force $\mathbf{s}$ and magnetic field unit vector $\mathbf{b}$ are defined in an x–y–z coordinate system; (ii) secondly, two further vectors orthogonal to $\mathbf{b}$ are formed, namely $\mathbf{b}\times\mathbf{s}$ and $\mathbf{b}\times(\mathbf{s}\times\mathbf{b})$; (iii) thirdly, the vector $\mathbf{b}$ is re-scaled to a length $|\mathbf{b}(\mathbf{b}\cdot\mathbf{s})|$ so that $\mathbf{s}=\mathbf{b}(\mathbf{b}\cdot\mathbf{s})+\mathbf{b}\times(\mathbf{s}\times\mathbf{b})$. Here θ is the angle between $\mathbf{s}$ and $\mathbf{b}$.

2.1. Super-Gaussian effects in the thermal energy equation

A useful approach to thinking about the $\underline{\underline{\phi}}^c$ coefficient is to expand equation (5) using $\nabla P_\mathrm{e}=n_\mathrm{e}\nabla T_\mathrm{e}+T_\mathrm{e}\nabla n_\mathrm{e}$, such that $\mathbf{q}=-\frac{n_\mathrm{e}\tau_\mathrm{B}T_\mathrm{e}}{m_\mathrm{e}}(\underline{\underline{\kappa}}^c+\underline{\underline{\phi}}^c)\cdot\nabla T_\mathrm{e}-\underline{\underline{\psi}}'\cdot\mathbf{j}\frac{T_\mathrm{e}}{e}-\frac{\tau_\mathrm{B}T_\mathrm{e}^2}{m_\mathrm{e}}\underline{\underline{\phi}}^c\cdot\nabla n_\mathrm{e}$, and then to consider its contribution to the energy equation, i.e.

$$\frac{3}{2}n_\mathrm{e}\frac{\partial T_\mathrm{e}}{\partial t}+\nabla\cdot\mathbf{q}-\mathbf{E}\cdot\mathbf{j}=\dot{U}_\mathrm{L}, \tag{7}$$

where the terms $\mathbf{E}\cdot\mathbf{j}$ and $\dot{U}_\mathrm{L}$ describe the rate-of-change of thermal energy $U=\frac{3}{2}n_\mathrm{e}T_\mathrm{e}$ due to Ohmic heating and laser heating respectively, and we have neglected hydrodynamical effects so that $\partial n_\mathrm{e}/\partial t=0$. Two consequences immediately present themselves which we consider below: firstly, modifications $\underline{\underline{\kappa}}^c\rightarrow\underline{\underline{\kappa}}^c+\underline{\underline{\phi}}^c$ to the conductive heat-flow $\mathbf{q}_\kappa\propto-\nabla T_\mathrm{e}$ and its associated phenomena; and secondly, the introduction of a new heat-flow term $\mathbf{q}_\phi\propto\underline{\underline{\phi}}^c\cdot\nabla n_\mathrm{e}$, which has the perpendicular component $\mathbf{q}_\mathrm{n}\propto\phi_\perp\nabla n_\mathrm{e}$.

2.1.1. Conductive heat-flow. Though familiar in its basic un-magnetized form, the conductive heat-flow is a good place to begin our discussion, since in magnetized plasmas it gives rise to other less well known phenomena considered in section 2.2.1. In particular, in the presence of magnetic fields (and with reference to equation (6)) this term may be separated into two components, viz.

$$\begin{aligned}\mathbf{q}_\kappa&=-\frac{\tau_\mathrm{B}P_\mathrm{e}}{m_\mathrm{e}}(\underline{\underline{\kappa}}^c+\underline{\underline{\phi}}^c)\cdot\nabla T_\mathrm{e}=\mathbf{q}_\perp+\mathbf{q}_\wedge,\quad\text{where}\\ \mathbf{q}_\perp&=-\frac{\tau_\mathrm{B}P_\mathrm{e}}{m_\mathrm{e}}(\kappa_\perp^c+\phi_\perp^c)\nabla T_\mathrm{e}\quad\text{and}\quad\mathbf{q}_\wedge=-\frac{\tau_\mathrm{B}P_\mathrm{e}}{m_\mathrm{e}}(\kappa_\wedge^c+\phi_\wedge^c)\mathbf{b}\times\nabla T_\mathrm{e}\end{aligned} \tag{8}$$

are the diffusive and Righi–Leduc heat-flows respectively. The motivation behind the first of these names is understood by considering its impact on thermal evolution, indeed, retaining this term only in equation (7), and temporarily taking $\nabla n_\mathrm{e}=0$, we have

$$\left[\frac{\partial T_\mathrm{e}}{\partial t}\right]_{\mathbf{q}_\perp}=\nabla\cdot(d_\mathrm{T}\nabla T_\mathrm{e}),\quad\text{where}\quad d_\mathrm{T}=\frac{c_\mathrm{B}}{3}\frac{\lambda_\mathrm{T}^2}{\tau_\mathrm{T}}(\kappa_\perp^c+\phi_\perp^c) \tag{9}$$

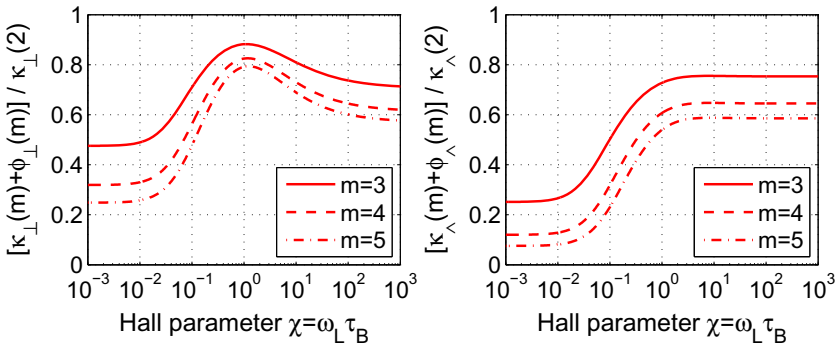

Figure 3. Suppression of both the diffusive thermal conductivity (left), and the Righi–Leduc heat-flow (right), visualized by plotting the respective ratios $[\kappa^c_\perp(m)+\phi^c_\perp(m)]/\kappa^c_\perp(2)]$ and $[\kappa^c_\wedge(m)+\phi^c_\wedge(m)]/\kappa^c_\wedge(2)]$ against χ for different values of super-Gaussian power m. In the low χ limit, these plots indicate suppression of thermal diffusion by ∼80% and the Righi–Leduc heat-flow by ∼90% when $m = 5$.

and $\lambda_T = v_T\tau_T$ is the thermal mean-free-path, i.e. a diffusion equation with *thermal diffusion coefficient* d_T. The second heat-flow component, the Righi–Leduc heat-flow $\mathbf{q}_\wedge$, represents that part of the thermal flux deflected due to the Lorentz force acting on negatively charged electrons, and is thus perpendicular to both ∇T_e and B. Because $\mathbf{q}_\wedge \propto \mathbf{b}\times\nabla T_e$ transports heat along isotherms, its impact on overall thermal evolution is often unclear; however, as we shall see in section 4, this term can be instrumental in driving instability [18, 24, 25, 29, 30].

In classical transport theory, with super-Gaussian power $m = 2$, neither $\mathbf{q}_\perp$ nor $\mathbf{q}_\wedge$ contain components arising from $\underline{\underline{\phi^c}}$ (because $\underline{\underline{\phi^c}} = \underline{\underline{0}}$). Consequently, the impact of super-Gaussian transport on the diffusive and Righi–Leduc heat-flows may be assessed by comparing the components of $[\underline{\underline{\kappa^c}}(m)+\underline{\underline{\phi^c}}(m)]$ with those of $[\underline{\underline{\kappa^c}}(2)+\underline{\underline{\phi^c}}(2)]$ for different values of $m \neq 2$. Indeed, doing so we find that super-Gaussian effects lead to reduction of thermal diffusion and the Righi–Leduc heat-flow by as much as ∼80 and ∼90% respectively (see figure 3 and table 1). Physically this corresponds to super-Gaussian broadening of the distribution function and the fact that heat-flow in laser plasmas is dominated by comparatively small numbers of high energy electrons travelling at ∼3–4v_T [31, 32]. By preferentially heating slower, more collisional electrons, IB results in a relative reduction in the number of high-energy electrons in the tail of the distribution (see figure 1) and a consequent lowering in the overall energy-flux compared to classical transport ($m = 2$) for otherwise equivalent conditions.

2.1.2. Heat-flow up density gradients. Mathematically, one of the reasons why the conductive heat-flow is so heavily suppressed by IB super-Gaussian distortions is that while the components of $\underline{\underline{\kappa^c}}$ are positive, those in $\underline{\underline{\phi^c}}$ are negative (see, for example, table 1; though plots of all the coefficients are given by Ridgers *et al* [14]). Curiously, this means that the $\phi^c_\perp$ coefficient can lead to a heat-flow $\mathbf{q}_n$ in the direction of ∇n_e:

$$\mathbf{q}_n = -\frac{\tau_B T_e^2}{m_e}\phi^c_\perp \nabla n_e = \frac{\tau_B T_e^2}{m_e}|\phi^c_\perp|\nabla n_e, \tag{10}$$

while $\phi_\wedge$ naturally yields a cross gradient component in $\mathbf{b}\times\nabla n_e$ (see equation (6)). The link between this new heat-flow effect and the underlying super-Gaussian distribution $f_{SG}(m)$ will be discussed further in section 3.3, and for the time being it is sufficient to note that the absence of $\underline{\underline{\phi}}^c$ in classical transport theory corresponds to exact cancellation of fluxing terms arising from the distribution function when $m=2$, i.e. given Gaussian f_0 (see, for example, Kruer [32]). Though a directly intuitive insight into the meaning of heat-flow up density gradients would be ideal, we shall see in section 2.2.3 that even without this knowledge $\mathbf{q}_n$ provides an interpretation for a new isothermal super-Gaussian advection phenomenon in the direction of increasing density.

2.2. *Super-Gaussian effects in the induction equation*

Proceeding along similar lines to those in section 2.1, the consequences of the $\underline{\underline{\gamma}}^c$ coefficient may be considered by looking at its contribution to the induction equation, itself found after substituting equation (4) into Faraday's Law $\nabla\times\mathbf{E}=-\partial\mathbf{B}/\partial t$, that is,

$$\frac{\partial\mathbf{B}}{\partial t}=\nabla\times\left[\underline{\underline{\gamma}}^c\cdot\frac{T_e\nabla n_e}{en_e}-\frac{\mathbf{j}\times\mathbf{B}}{en_e}-\frac{m_e}{n_e e^2\tau_B}\underline{\underline{\alpha}}^c\cdot\mathbf{j}+\frac{1}{e}(\underline{\underline{\beta}}^c+\underline{\underline{\gamma}}^c)\cdot\nabla T_e\right], \tag{11}$$

where we have used $\nabla P_e=n_e\nabla T_e+T_e\nabla n_e$. As in section 2.1, two initial features are clear: firstly, modifications to the thermoelectric tensor relative to the classical transport case ($\underline{\underline{\beta}}^c+\underline{\underline{\mathbf{I}}}\rightarrow\underline{\underline{\beta}}^c+\underline{\underline{\gamma}}^c$), especially in the cross-field '$\wedge$' terms; and secondly, new effects arising from $\underline{\underline{\gamma}}^c$ in the ∇n_e term. Both of these are considered further below.

2.2.1. Suppression of the Nernst effect. For our current purposes, the key component of the thermoelectric tensor ($\underline{\underline{\beta}}^c+\underline{\underline{\gamma}}^c$) in equation (11) is the cross field term in $\mathbf{b}\times\nabla T_e$ (see equation (6)), since it is this part which describes advection of the magnetic field by the Nernst effect [33]. Indeed, retaining just this term we obtain the advection equation [18]

$$\left[\frac{\partial\mathbf{B}}{\partial t}\right]_{\beta^c_\wedge}=\nabla\times(\mathbf{v}_N\times\mathbf{B})\quad\Rightarrow\quad\left[\frac{\partial B}{\partial t}\right]_{\beta^c_\wedge}+\nabla\cdot(\mathbf{v}_N B)=0,$$

$$\text{where}\quad\mathbf{v}_N=-a_N\frac{\nabla T_e}{T_e},\quad a_N=\frac{c_B}{2\chi}\frac{\lambda_T^2}{\tau_T}(\beta^c_\wedge+\gamma^c_\wedge), \tag{12}$$

$\lambda_T=v_T\tau_T$ is the thermal mean-free-path, and the implied expression follows from our geometric considerations in a Cartesian coordinate system with $\mathbf{B}=B\hat{\mathbf{z}}$ and $B=|\mathbf{B}|$. Here $\mathbf{v}_N$ is the Nernst advection velocity (cf reference [33]) which carries the magnetic field down temperature gradients (in the direction $-\nabla T_e$) and that we have chosen to define in terms of a *Nernst advection coefficient* a_N [18]. The 'old' $\beta^c_\wedge$ coefficient is reduced in the super-Gaussian theory; however, because $\gamma^c_\wedge$ is negative, the Nernst velocity is further suppressed by the new coefficient. Indeed, for the case where $m=5$, when $\gamma^c_\wedge$ is of a similar order to $\beta^c_\wedge$ [14], we see as much as a five-fold reduction in the Nernst velocity in the low χ limit (see figure 4). This reduction naturally follows from the physical interpretation of the Nernst effect as advection of the magnetic field with the diffusive heat-flow $\mathbf{q}_\perp$ [20, 31, 33], an inference made explicit by writing

$$\mathbf{v}_N=\frac{(\beta^c_\wedge+\gamma^c_\wedge)}{\chi(\kappa^c_\perp+\phi^c_\perp)}\frac{\mathbf{q}_\perp}{P_e}=\frac{2a_N}{3d_T}\frac{\mathbf{q}_\perp}{P_e}\approx\frac{2}{3}\frac{\mathbf{q}_\perp}{P_e}, \tag{13}$$

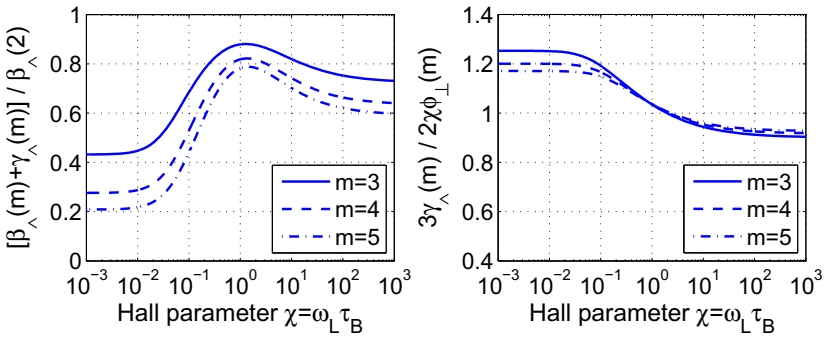

Figure 4. Suppression of the Nernst effect (left) visualized by plotting $[\beta^c_\wedge(m) + \gamma^c_\wedge(m)]/\beta^c_\wedge(2)$ as a function of χ for different values of super-Gaussian power m. Note that this ratio is $\sim$0.2 in the limit of low χ implying suppression by a factor of five. The right-hand plot depicts $3\gamma^c_\wedge/2\chi\phi^c_\perp \approx 1$ as a function of χ, and suggests an interpretation for the new *anomalous Nernst* advection effect described in section 2.2.3.

where $\mathbf{q}_\perp/\frac{3}{2}P_e$ is a characteristic velocity of energy flow (recall that $\frac{3}{2}P_e = \frac{3}{2}n_eT_e$ is the energy density) and we have noted the approximate equality $a_N \approx d_T$ [18, 29]. Because the diffusive heat-flow is suppressed in the super-Gaussian transport theory, the Nernst effect is reduced by an almost identical amount (compare figures 3 and 4).

2.2.2. Suppression of magnetic field generation by the $\nabla T_e \times \nabla n_e$ mechanism. The super-Gaussian coefficient $\underline{\underline{\gamma^c}}$ has two main consequences for the ∇n_e term in the induction equation: firstly, suppression of the $\nabla T_e \times \nabla n_e$ field generation mechanism [34, 35], a key source of magnetic field in laser–plasmas [3, 36, 37]; and secondly, the introduction of a new field advection effect (see section 2.2.3). Retaining just this part we find

$$\left[\frac{\partial \mathbf{B}}{\partial t}\right]_{\underline{\underline{\gamma^c}}} = \nabla \times \left[\frac{\gamma^c_\perp T_e \nabla n_e}{e n_e} - \frac{\gamma^c_\wedge T_e}{e n_e}\nabla n_e \times \mathbf{b}\right] \tag{14}$$

(see equation (6)), so that by evaluating the first term on the right-hand side, and neglecting gradients in $\gamma^c_\perp$, we obtain a new expression for the $\nabla T_e \times \nabla n_e$ mechanism:

$$\left[\frac{\partial \mathbf{B}}{\partial t}\right]_{\gamma^c_\perp} = \gamma^c_\perp \frac{\nabla T_e \times \nabla n_e}{e n_e}. \tag{15}$$

For $m = 5$ we have $\gamma^c_\perp \in (0.7, 1.0]$ (see table 1), so that magnetic field generation can be suppressed by as much as $\sim$30% in the super-Gaussian theory [14].

2.2.3. New isothermal 'anomalous Nernst' advection effect. In a similar fashion to that described above, by taking the curl of the second term on the right-hand-side of equation (14) we arrive at the advection equation

$$\left[\frac{\partial \mathbf{B}}{\partial t}\right]_{\gamma^c_\wedge} = \nabla \times \left(\mathbf{v}_\gamma \times \mathbf{B}\right) \quad \Rightarrow \quad \frac{\partial B}{\partial t} + \nabla \cdot (\mathbf{v}_\gamma B) = 0,$$

$$\text{where} \quad \mathbf{v}_\gamma = -a_\gamma \frac{\nabla n_e}{n_e} \quad \text{and} \quad a_\gamma = \frac{c_B}{2\chi}\frac{\lambda_T^2}{\tau_T}\gamma^c_\wedge \tag{16}$$

is an *advection coefficient* [18] (cf equation (12)). Consequently, $\gamma_\wedge^c$ is understood to introduce advection of the magnetic field with velocity $\mathbf{v}_\gamma$. This new advection phenomena is a direct isothermal analogue of the Nernst effect (see section 2.2.1) and, since

$$\mathbf{v}_\gamma = \frac{\gamma_\wedge^c}{\chi \phi_\perp^c} \frac{\mathbf{q}_\mathrm{n}}{P_\mathrm{e}} \approx \frac{2}{3} \frac{\mathbf{q}_\mathrm{n}}{P_\mathrm{e}}, \tag{17}$$

where the approximate equality follows from figure 4, may be interpreted as advection of magnetic field with the new density-gradient driven heat-flow $\mathbf{q}_\mathrm{n}$ (see equations (10) and (13)). Note that $\gamma_\wedge^c$ is negative (again, see [14]), so $\mathbf{v}_\gamma \propto \nabla n_\mathrm{e}$ carries field into regions of *higher* density. Given its similarity to the Nernst effect, we shall refer to this advection phenomena as the *anomalous Nernst effect*, with a_γ as the *anomalous Nernst advection coefficient*[7].

2.3. Summary of super-Gaussian transport effects

In the previous sections we have seen that the super-Gaussian transport theory acts to suppress classical effects, especially in the case of strong IB for which $m = 5$, while simultaneously introducing new phenomena. These results are summarized as follows:

- Suppression of the diffusive heat-flow by up to $\sim$80%.
- Suppression of the Righi–Leduc heat-flow by up to $\sim$90%.
- Introduction of a new heat-flow term $\mathbf{q}_\mathrm{n}$ in the direction of increasing density ∇n_e.
- Suppression of the Nernst effect by up to $\sim$80%.
- Suppression of the $\nabla T_\mathrm{e} \times \nabla n_\mathrm{e}$ source term by up to $\sim$30%.
- Introduction of an isothermal *anomalous Nernst* advection effect with $\mathbf{q}_\mathrm{n} \propto \nabla n_\mathrm{e}$.

In all cases, classical transport effects are reduced most heavily in the limit $\chi \to 0$ (see figures 3 and 4). Note that while the comparisons presented in this section have been made in the Lorentz approximation ($Z \to \infty$), it would be straightforward to repeat them after generalizing the theory to arbitrary Z (see section 5 and appendix C).

3. Kinetic study of the new transport effects

So far our discussion of super-Gaussian transport phenomena has been limited to a fluid perspective, and it is important that we also verify them in a 'first principles' fashion through kinetic analysis and simulation. Consequently, we now demonstrate that the new density-gradient driven heat-flow (section 2.1.2), and associated anomalous Nernst effect (section 2.2.3),

[7] This is not to be confused with the Ettingshausen effect in $\psi_\wedge$, which is also isothermal, but describes advection of *thermal* energy down *magnetic field* gradients. Indeed, keeping only the Ettingshausen heat-flow $\mathbf{q}_\mathrm{E} = -\psi_\wedge(T_\mathrm{e}\mathbf{b} \times \mathbf{j}/e)$ in equation (7), one obtains the advection equation (cf equation (12))

$$\frac{\partial T_\mathrm{e}}{\partial t} + \nabla \cdot (\mathbf{v}_\mathrm{E} T_\mathrm{e}) = 0, \quad \text{where} \quad \mathbf{v}_\mathrm{E} = -a_\mathrm{E} \frac{\nabla B}{B} \quad \text{and} \quad a_\mathrm{E} = \frac{2\chi}{3c_\mathrm{B}} \frac{\delta^2}{\tau_\mathrm{T}} \psi_\wedge$$

are in Bissell's notation the *Ettingshausen velocity* and *Ettingshausen advection coefficient* respectively [18], while the skin-depth δ is defined in equation (28). The Ettingshausen effect is naturally considered the reverse analogue of Nernst, with $\psi_\wedge(2) = \beta_\wedge(2)$ in classical transport theory ($m = 2$).

appear in full blown kinetic simulations using our VFP code IMPACT [23] (sections 3.1 and 3.2). A simplified kinetic analysis, to physically motivate the emergence of ∇n_e driven heat-flux when $m > 2$, is also presented (section 3.3).

In essence, the VFP simulations detailed here follow a similar procedure to those of Ridgers *et al* [14]; however, rather than fixing the isotropic part of the distribution function f_0 to an exact super-Gaussian f_{SG} (see equation (1)), we allow f_0 to evolve dynamically at each point in space. Two approaches which respectively exclude (section 3.1) and include (section 3.2) continual IB heating shall be shown: in the first, we employ an artificial collision operator permitting selection of $m \in [2, 5]$, and let f_0 relax to a super-Gaussian f_{SG} via electron–electron collisions; while in the second, we use Langdon's IB heating operator to distort the distribution function in the usual way, i.e. by preferentially transmitting energy to the more collisional, low velocity bulk of the distribution function [16]. Note that the former method corresponds most closely to the theoretical work in section 2, since the artificial electron–electron collisions tend to drive f_0 towards f_{SG} exactly; for the later (heating) simulations, which use the real electron–electron collision operator, competition between IB distortion (forcing $2 \leqslant m \leqslant 5$), collisional relaxation ($m \to 2$), and spatial transport in the tail of the distribution ($m \to 2$), means that taking f_0 to be super-Gaussian f_{SG} is more approximate [14, 40].

Indeed, non-local transport is expected to distort the distribution function from an exact super-Gaussian in both sets of simulations. Fortunately, however, one expects $f_0 \approx f_{SG}$ under highly collisional conditions, and the VFP simulations should recover super-Gaussian transport in this limit (or classical transport if $m = 2$). For characteristic length-scales l_ϕ, given in three-dimensions by $|l_\phi| = |\phi|/|\nabla\phi|$, where $\phi \in \{T_e, n_e, B\}$ (cf equation (29)), and for typical collisional transport time-scales τ_{CT}, the highly collisional limit is defined by the strong inequalities $\lambda_T \ll |l_\phi|$ and $\tau_T \ll \tau_{CT}$; for periodic perturbations with wave-number k, one also requires $k\lambda_T \ll 1$.

3.1. Super-Gaussian transport in idealized Vlasov–Fokker–Planck simulation

Our first set of IMPACT simulations, designed to verify the emergence of new transport effects from the underlying kinetic dynamics, involve relaxing the isotropic part of the distribution function f_0 to a super-Gaussian via an artificial electron–electron collision operator $[\partial f_0/\partial t]_C(m)$ with selectable index m. The theoretical implementation of this operator is discussed in appendix A; here it suffices to say that if IMPACT is initialized with some arbitrary distribution, e.g. the classical Gaussian form $f_0(t = 0) = f_{SG}(2)$, and if the generalized electron–electron collision operator is set to some super-Gaussian index m, then collisional relaxation will drive $f_0 : f_{SG}(2) \to f_{SG}(m)$. We refer to this set of calculations as *idealized VFP kinetic simulations* (figures 5 and 6).

3.1.1. Simulation details. The specific one-dimensional verification simulations were based on x-directed perturbation calculations, with atomic number $Z = 10$, background density n_0, and initial uniform temperature T_0 chosen such that the initial thermal velocity v_0 and plasma frequency ω_{pe} (defined in equation (28)) gave $v_0/c = 1/10$ and $\omega_{pe} = 100/\tau_0$ respectively, where c is the speed of light *in vacuo* and $\tau_0 = \tau_T(T_0, n_0)$ is the initial thermal collision time. (These values correspond to typical conditions of hot plasma, at or below critical density, during intense nanosecond duration laser–plasma interactions, see appendix B.) In this way, we studied the new transport effects on a system of length $L_x = 1000\lambda_0$ (where $\lambda_0 = v_0\tau_0$) as

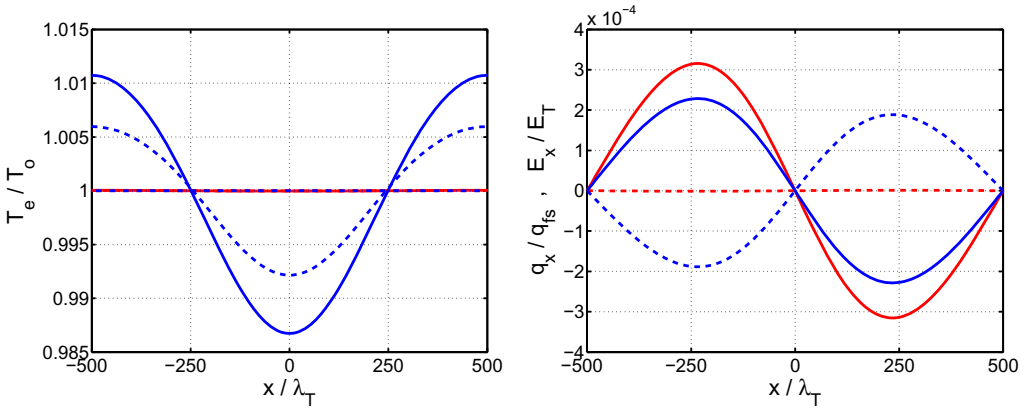

Figure 5. Left: evolution of $T_e(x)$ from 'idealized' VFP kinetic simulations, for a static, 10% modulated density profile $\delta n_e(x) = -0.1 n_0 \cos(2\pi x/L_x)$, where $L_x = 1000\lambda_0$. The $m = 2$ (red) simulation shows isothermal conditions being almost exactly maintained, whilst for the $m = 5$ (blue) case, a temperature modulation develops in phase with the density perturbation. Times shown are $t = 0$, 5000 and $10\,000\tau_0$ (dash-dotted, dashed and solid, respectively). Right: heat-flow q_x in units of the free-streaming limit $q_{fs} = \frac{1}{2} n_0 m_e v_0^3$ (dashed), and electric field E_x in units of $E_T = (m_e/e)\lambda_0/\tau_0^2$ (solid), both at $t = \tau_0$, for $m = 2$ (red) and $m = 5$ (blue).

they arose from a harmonic density modulation $n_0 = n_e + \delta n_e$, with 10% perturbation $\delta n_e(x) = -0.1 n_0 \cos(2\pi x/L_x)$. In an attempt to minimize numerical errors, these simulations employed a relatively detailed velocity resolution $\Delta v = v_0/40$ (i.e. a velocity domain $v \in [0, 6v_0]$ gridded by $n_v = 240$ cells), a small time-step $\Delta t = 0.2\tau_0$, and a uniform spatial grid of $n_x = 160$ cells.

To compare super-Gaussian transport effects ($m > 2$) with classical results ($m = 2$), the distribution function was initialized at either $m = 2$ or 5 throughout the domain, and an identical index used in our artificial collision operator $[\partial f_0/\partial t]_C(m)$; in this way the isotropic part of the distribution function f_0 was (broadly speaking) 'clamped' at its initial super-Gaussian power as the system evolved (see appendix A.1). Both unmagnetized and magnetized conditions were considered; for the latter, $\mathbf{B} = B\hat{\mathbf{z}}$ was set to an initial value $B = B_z = B_{z0} = 10^{-4}\,(m_e/e\tau_0)$, which corresponds to an initial Hall parameter $\chi_0 = 10^{-4} c_B \approx 10^{-4}$, where $c_B = 3\sqrt{\pi}/4$ as defined in section 1.

3.1.2. Results. Figure 5 (right) shows that heat q_x does indeed flow up gradients in the harmonic density perturbation $\delta n(x)$ when $m = 5$ (blue curves), as predicted in section 2.1.2, leading to a growing temperature perturbation in phase with $\delta n_e(x)$; these features are absent when IMPACT is run with the classical (Gaussian) electron distribution function $m = 2$ (red curves). In fact due to numerical errors associated with the finite differencing, there is a slight numerical heat-flow q_x when $m = 2$; however, this flux is very small, perturbing T_e by only about 3×10^{-3}% at $t = 10\,000\tau_0$, and is negligible when compared to the physical effect shown for $m = 5$, which modulates the temperature by about 1% over the same period (see figure 5, left). A comparison of the electric field E_x for $m = 2$ and 5 just after $t = 0$ (at $t = \tau_0$) is also shown (figure 5, right). Note that while the results depicted in figure 5 are for an unmagnetized

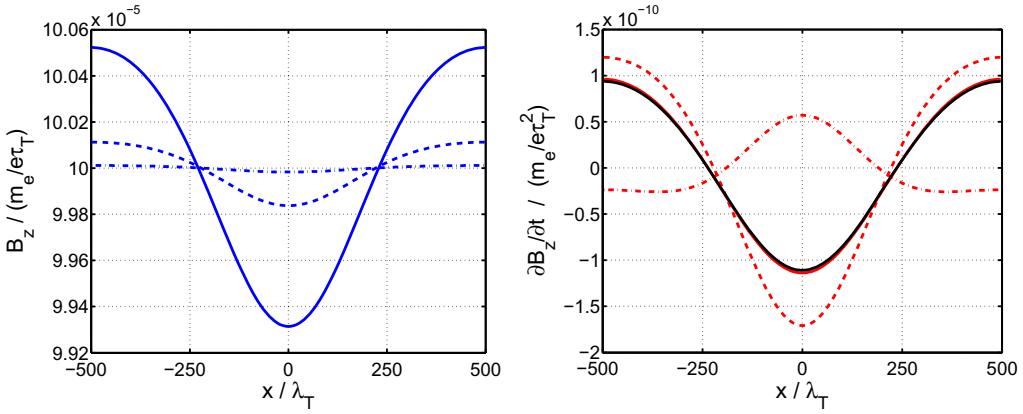

Figure 6. Anomalous Nernst advection of magnetic field from 'idealized' VFP kinetic simulation with $m = 5$. These simulation conditions correspond to those shown in figure 5, but in this case the plasma is initialized with a uniform field $B_{z0} = 10^{-4}(m_e/e\tau_0)$. Left: evolution of the magnetic field $B = B_z(x)$. Times shown are $t = 100$, 1000 and $5000\tau_0$ (dash-dotted, dashed and solid, respectively). Right: magnetic induction $\partial B_z/\partial t = -\nabla \times \mathbf{E}$ at $t = 5000\tau_0$ as predicted by both simulation (black), and the super-Gaussian theory (red), where the curves describe temporal evolution of $\mathbf{B}$ due to: (i) anomalous Nernst $\mathbf{v}_\gamma \propto \nabla n_e$ (dashed); (ii) conventional Nernst $\mathbf{v}_N \propto -\nabla T_e$ (dash-dotted); and (iii) all terms in Ohm's law, i.e. equation (4) (solid). Theoretical values are calculated from Ohm's law (equation (4)) using instantaneous $T_e(x)$, $n_e(x)$ and $\chi(x)$ simulation profiles, and polynomial fits to the super-Gaussian transport coefficients given by Ridgers *et al* [14].

plasma, virtually identical results are obtained in the weakly magnetized case with $\chi_0 \approx 10^{-4}$. (One observes these phenomena for other super-Gaussian indices too (our range also included $m \in \{2.1, 3.0, 4.0, 4.5\}$), but the effect decreases monotonically with m.)

The idealized VFP calculations suggest that $T_e(x)$ is exponentially relaxing to steady-state, despite persistent $\mathbf{q}_n$ heat-flux; though such an effect is not obvious from the $100\,00\tau_0$ simulations shown here because their duration is comparable to only a single e-folding time. Nevertheless, one can follow the temporal evolution of the thermal profile further by initializing IMPACT with coarser resolution, and in this case the system does appear to approach a steady-state ($\partial T_e/\partial t = 0$), with matched—but opposing—diffusive ($\mathbf{q}_\perp$) and density-gradient driven ($\mathbf{q}_n$) heat-flows.

When a magnetic field is added to the system, the density-gradient driven heat-flow leads to advection of the magnetic field via the anomalous Nernst effect described theoretically in section 2.2.3 (figure 6, left-hand plot). Indeed, at $t = 5000\tau_0$, when the anomalous Nernst effect dominates field transport, the temporal evolution of $B = B_z$ measured from IMPACT compares well (to within approximately 1%) with that predicted by the super-Gaussian theory. Modulation of the thermal profile $\delta T_e(x)$ by $\mathbf{q}_n$ inevitably gives rise to some conventional $\mathbf{v}_N \propto -\nabla T_e$ Nernst advection which partially counteracts the density-gradient driven advection with $\mathbf{v}_\gamma \propto \nabla n_e$. However, at earlier times before δT_e develops, anomalous Nernst dominates heavily, and is therefore chiefly responsible for the periodic field evolution shown here; all other induction

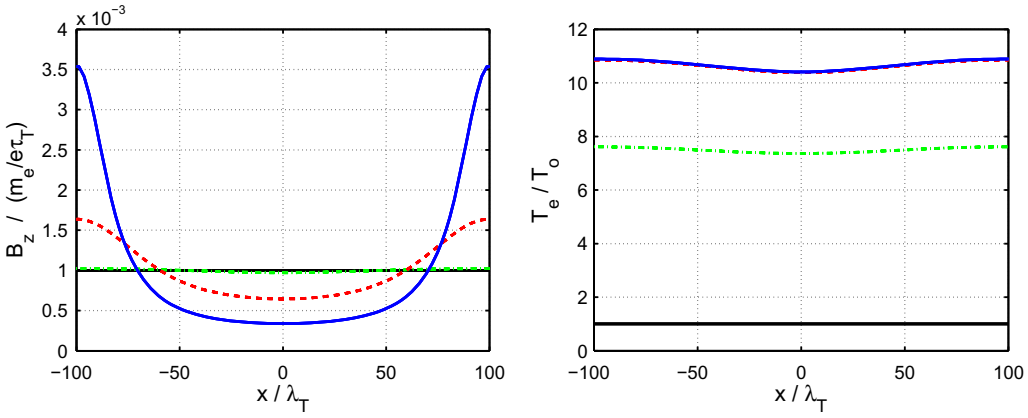

Figure 7. Demonstration of super-Gaussian transport effects as a plasma with (static) 10% modulated density $\delta n_e(x) = -0.1 n_0 \cos(2\pi x/L_x)$, and initially uniform magnetic field $B = B_{z0} = 10^{-3}(m_e/e\tau_0)$, is subject to IB heating. Here the IB heating intensity corresponds to the 'strong' case of $v_{osc.}/v_0 = 1/\sqrt{2}$. Left: evolution of the magnetic field $B = B_z(x)$ due to the dominance of anomalous Nernst advection over conventional Nernst (note how the field is carried into the hotter region, see right). Right: evolution of $T_e(x)$ due to both the density dependence of IB heating, and the novel heat-flow $\mathbf{q}_n \propto \nabla n_e$. Times shown are $t = 0$, 500, 2500 and $5000\tau_0$ (black—solid, green—dash-dotted, red—dashed, and blue—solid, respectively).

sources (see equation (11)) either vanish upon taking the curl, or are negligible. Indeed, the close agreement between the numerically determined $\partial B_z/\partial t$, and our theoretical calculations (figure 6, right-hand plot), serves to verify that the new ∇n_e driven phenomena predicted in section 2 are correct when m is fixed, at least to first-order in $\lambda_T/|l_n|$ and $\lambda_T/|l_T|$, where the IMPACT simulations are expected to be valid.

3.2. Super-Gaussian transport arising from inverse bremsstrahlung heating

Our second set of simulations demonstrate both density-gradient driven heat-flow $\mathbf{q}_n$, and associated anomalous Nernst advection, in the more realistic situation of a plasma subject to IB heating (figures 7 and 8). In this case the electron distribution function is distorted towards a super-Gaussian by the heating mechanism itself [16] (see appendix A.2), so the real electron–electron collision operator, which relaxes f_0 to a Gaussian, i.e. $f_0 \to f_{SG}(2)$, is used throughout. Unlike the simulations described in section 3.1, therefore, this second set does not rely on unphysical assumptions; moreover, they allow for distortion to f_0 due to non-local transport (if present) arising from super-thermal electrons with very long mean-free-paths and thermalization times.

3.2.1. Simulation details. The one-dimensional IB heating simulations were initialized as above (section 3.1.1), that is, with atomic number $Z = 10$, uniform temperature T_0, and a 10% harmonic density modulation $\delta n_e(x) = -0.1 n_0 \cos(2\pi x/L_x)$, such that $v_0/c = 1/10$ and $\omega_{pe}\tau_0 = 100$. In this case, however, slightly stronger magnetization was considered, and

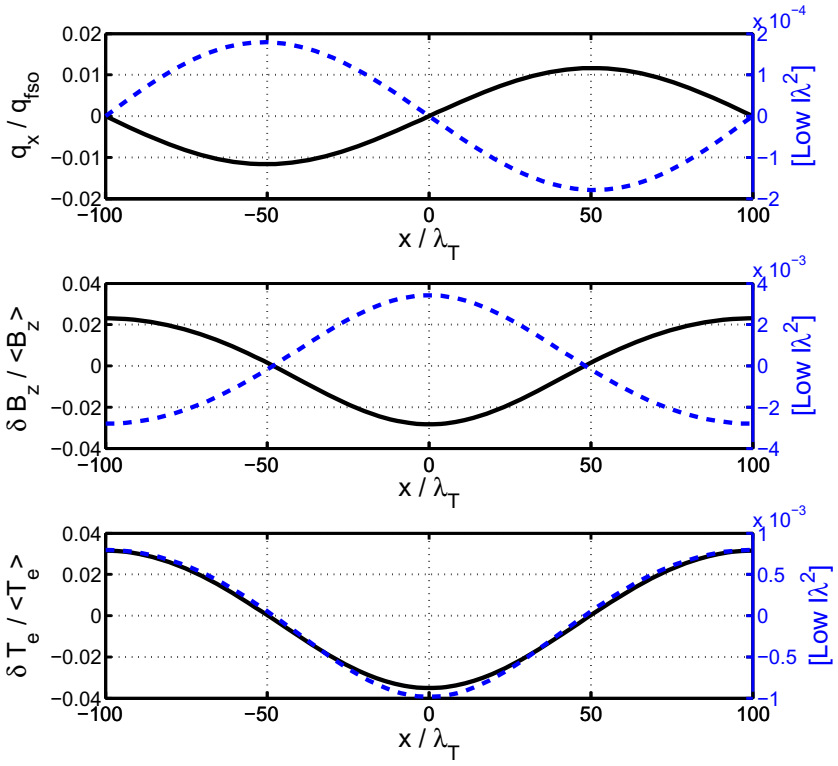

Figure 8. Comparison of the effect of high power ($v^2_{\text{osc.}}/v^2_0 = 0.5$, black curves, left y-axis), and low power ($v^2_{\text{osc.}}/v^2_0 = 0.005$, dotted blue curves, right y-axis) IB heating on the total heat-flow q_x (top), magnetic field B_z (middle) and temperature T_e (bottom), at $t = 500\tau_\text{T}$. The perturbations δT_e and δB_z relate to domain averaged quantities (angle brackets), while $q_{\text{fs}0} = q_\text{fs}(T_\text{e}/T_0)^{3/2}$ is the local 'free streaming' heat-flow ($q_\text{fs} = \frac{1}{2}n_0 m_\text{e} v_0^3$ was defined in figure 5).

the plasma initially embedded with a weak, uniform magnetic field $B_{z0} = (m_\text{e}/e\tau_0)10^{-3}$, corresponding to $\chi_0 = (3\sqrt{\pi}4) \times 10^{-3} \approx 10^{-3}$. Furthermore, the different numerical demands for the heating runs meant that this time we adopted a periodic system of length $L_x = 200\lambda_0$, and spatial, temporal, and velocity resolutions $n_x = 80$, $\Delta t = 0.2\tau_0$, and $n_v = 120$ respectively, with velocity domain $v \in [0, 6v_0]$. Note that because IMPACT's Langdon IB heating operator distorts f_0 towards a super-Gaussian in a physically consistent fashion [16] (see equation (A.6), appendix A.2)), the electron distribution function was initialized with $m = 2$ throughout.

For comparison of super-Gaussian phenomena under different laser intensities, two sets of heating runs were considered: a 'weak' case with $v_{\text{osc.}}/v_0 = 1/\sqrt{200}$; and a 'strong' case for which $v_{\text{osc.}}/v_0 = 1/\sqrt{2}$. In both instances the quiver velocity $v_{\text{osc.}}$ of equation (3) was set to be spatially uniform, and the heating phased in at time $t = 50\tau_0$ using a throttling function $[1 + \tanh(t/\tau_w)]/2$ with width $\tau_w = 5\tau_0$.

3.2.2. Results. During 'strong' IB heating with $v_{\text{osc.}}/v_0 = 1/\sqrt{2}$, magnetic field is pushed from the density troughs towards the density peaks due to the anomalous Nernst effect, while the overall plasma temperature rises (figure 7). As expected from the IB heating rate $(\partial T_\text{e}/\partial t)_\text{IB}$ for

the Gaussian index $m = 2$, that is,

$$\left(\frac{\partial T_e}{\partial t}\right)_{IB} = \frac{4}{9\sqrt{\pi}} \frac{m_e v_{osc.}^2}{\tau_T} \propto n_e T_e^{-3/2} \tag{18}$$

(see appendix A.2), the temperature initially rises rapidly, but then heating slows down due to its dependence on the collision time $\tau_T \propto T^{3/2}/n_e$. Notice from the right-hand plot in figure 7, that a temperature perturbation $T_e(x)$ develops during heating in phase with the density perturbation: this is partly caused by the IB heating density dependence $(\partial T_e/\partial t)_{IB} \propto n_e$, but also results from the new density-gradient driven $\mathbf{q}_n \propto \nabla n_e$ shown for $t = 500\tau_T$ in figure 8 (top, black—solid curve). Indeed, the total heat-flux q_x, which peaks at about 0.05% of the *local* free-streaming value $q_{fs0} = \frac{1}{2} n_0 m_e v_0^3 (T_e/T_0)^{3/2}$, is flowing *against* the temperature gradient, so must be dominated by $\mathbf{q}_n$ at this time.

Figure 8 also depicts $T_e(x)$, $B_z(x)$, and $q_x(x)$ for the 'weak' IB heating simulation where $v_{osc.}/v_0$ is 10 times smaller (equivalent to a 100 times weaker laser irradiance $I\lambda^2$, see equation (3)). In this case, heat-flow is directed down the temperature gradient, and the source of the temperature perturbation arises almost solely from the density dependence of IB heating, with $\mathbf{q}_\perp \propto -\nabla T_e$ dominated heat-flow acting to diffuse the perturbation (see section 2.1.1). As expected, this difference in the dominant heat-flow mechanism is reflected in the transport of magnetic field: for weak IB heating, conventional Nernst advection with velocity $\mathbf{v}_N \propto -\nabla T_e$ (see equation (12)) compresses field in the temperature trough; conversely, for strong IB heating, anomalous Nernst advection with velocity $\mathbf{v}_\gamma \propto \nabla n_e$ (see equation (16)) carries field *up* the density gradient, producing a perturbation in anti-phase to the weak heating case (see figure 8).

It is instructive to consider the super-Gaussian m indices arising in these simulations using comparable zero-dimension ($n_x = 1$) heating-runs, and by choosing electron number densities to match the one-dimensional density perturbation peak ($n_e = 1.1n_0$) and trough ($n_e = 0.9n_0$). For strong IB heating and $n_e = 0.9n_0$, this calculation gives $m \approx 3.9$, 3.6 and 3.3, at times $t = 100$, 200 and $500\tau_0$ respectively; while for higher density $n_e = 1.1n_0$, which heats faster, but has slightly lower $v_{osc.}/v_T$, the super-Gaussian index m takes marginally smaller values at corresponding times (e.g. $m \approx 3.2$ at $t = 500\tau_0$). In the weak-heating case, $m \approx 2.2$ at $t = 500\tau_0$.[8] The lack of observable anomalous Nernst and density-gradient driven heat-flow for $m \approx 2.2$, contrasting with their definite presence at $m > 3$, suggests that there may be a sharp threshold value for m above which these phenomena suddenly 'switch on'.

Finally, notice that while our calculations permit non-local distortion of f_0, the density gradient driven heat-flow and anomalous Nernst effect nonetheless dominate for strong IB heating. Though non-local distortion to f_0 has not been quantified here, the perturbation wavelength is easily small enough at later times (i.e. $L_x/\lambda_T \sim 200[T_0/T_e(t)]^2$) for non-local transport to occur. This suggests that super-Gaussian phenomena are robust for density perturbations up to the 10% level subject to relatively uniform heating; further work is needed to assess other configurations and conditions.

[8] Note that the actual distribution functions calculated by IMPACT do not exactly fit a unique $f_{SG}(m)$ over all velocity space, and the values stated correspond to good 'fits by eye' on log-linear plots. Indeed, the simulated f_0 tends to be have a higher effective m value for $v/v_T < 0.5$ than these fits; however, the low v region is less crucial to transport phenomena, so this discrepancy is not important.

3.3. Kinetic picture of density-gradient driven heat flow

Having considered the new phenomena numerically, we now present a simplified kinetic analysis to explain how heat-flow can arise from density gradients in otherwise isothermal plasmas, when the electron distribution function has a super-Gaussian form with $m \neq 2$. For simplicity, we neglect the effect of magnetic fields here, assert uniform super-Gaussian index m, and—as in our numerical study—restrict our analysis to a one-dimensional system in x. Assuming static ions, such that $\partial n_e/\partial t = 0$, we thus explore the new effects for some fixed, arbitrary density gradient $\nabla n_e \neq \mathbf{0}$.

For the isothermal, one-dimensional conditions considered, pressure gradients $\nabla P_e = T_e \nabla n_e$ associated with ∇n_e can only be maintained provided there exist some electric field $\mathbf{E} \propto -\nabla P_e/n_e \propto -T_e \nabla \log n_e$ to prevent diffusion of electrons (from high to low density) and subsequent concentration of charge. Indeed, it is this field which ensures a vanishing current $\mathbf{j} = \mathbf{0}$, and the preservation of quasi-neutrality (we require $\mathbf{j} = \mathbf{0}$ to maintain global $\nabla \cdot \mathbf{j} = \mathbf{0}$ since currents cannot circulate in one dimension). When $m = 2$, such a scenario cannot yield a heat-flow [32]; however, when $m \neq 2$, differences in the way that 'fast' and 'slow' electrons respond to each of the forcing terms—the density gradient and the electric field—can give rise to thermal transport. In fact, it is this disparity of response by electrons in different parts of the distribution function that lies at the heart of ∇n_e driven heat-flow, as we now demonstrate.

We begin our analysis in the usual way by expanding the electron distribution function $f(\mathbf{v}, \mathbf{r}, t)$ in terms of isotropic $f(\mathbf{r}, v, t)$ and anisotropic $\mathbf{f}_1(\mathbf{r}, v, t)$ components, such that $f = f_0 + \mathbf{f}_1 \cdot \mathbf{v}/v$ [38, 39]. Here f_0 is the part approximated by f_{SG} in the super-Gaussian transport theory [14], while $\mathbf{f}_1$ represents the first-order flux of electrons, and discriminates the contributions of different energy (speed v) groups to the net electron flux. In this way, f_0 accounts for bulk scalar quantities $\phi(v)$ associated with the velocity average $\langle\phi\rangle = \frac{4\pi}{n_e}\int_0^\infty \phi f_0 v^2\,\mathrm{d}v$ (such as temperature T_e and number density n_e); while $\mathbf{f}_1$ describes fluxing quantities $\mathbf{Q} = Q(v)\mathbf{v}/v$, which may be obtained using the velocity average $\langle\mathbf{Q}\rangle = \frac{4\pi}{3n_e}\int_0^\infty Q\mathbf{f}_1 v^2\,\mathrm{d}v$ (such as the electron current $\mathbf{j}$ and heat-flow $\mathbf{q}$) [38, 39].

In the Lorentz approximation (i.e. relative dominance of electron–ion angular scattering) with no magnetic field ($\mathbf{B} = \mathbf{0}$), $\mathbf{f}_1$ satisfies the (expanded VFP) $\mathbf{f}_1$-equation

$$v\nabla f_0 - \frac{e\mathbf{E}}{m_e}\frac{\partial f_0}{\partial v} = -\frac{\nu'_{ei}}{v^3}\mathbf{f}_1, \tag{19}$$

where $\nu'_{ei} = [(e^2/\epsilon_o m_e)^2/4\pi]Z^2 n_i \log\Lambda_{ei}$ is the velocity independent part of the electron–ion collisional scattering frequency $\nu_{ei}(v) = \nu'_{ei}/v^3$ (cf appendix A). For our stated assumptions ($\nabla T_e = \mathbf{0}$ and $\nabla n_e \neq \mathbf{0}$) the super-Gaussian distribution yields $\partial_v f_{SG}/\partial v = -m f_{SG} v^{m-1}/[\alpha_e(m) v_T]^m$ and $\nabla f_{SG} = f'_{SG}\nabla n_e$, where $f'_{SG} = f_{SG}/n_e$, so that by equation (19) with $f_0 = f_{SG}$, the x-component (f_x) of $\mathbf{f}_1$ is given by

$$f_x = -\frac{v^4}{\nu''_{ei}} f'_{SG}\frac{\partial \log(n_e)}{\partial x} - \frac{v^{2+m}}{\nu''_{ei}}\frac{m}{(\alpha_e v_T)^m} f'_{SG}\frac{eE_x}{m_e}, \tag{20}$$

where $\nu''_{ei} = \nu'_{ei}/n_e$ is the angular scattering frequency with both density and velocity dependence removed, and E_x is the x-component of $\mathbf{E}$. Equation (20) has the form

$$f_x = -D'\frac{\partial n_e}{\partial x} - \mu' n_e E_x,$$
$$\text{where} \quad D' = \frac{v^4 f'_{SG}}{\nu'_{ei}} \quad \text{and} \quad \mu' = \frac{v^{2+m} f'_{SG}}{\nu'_{ei}}\frac{m}{(\alpha_e v_T)^m}\frac{e}{m_e} \tag{21}$$

are coefficients describing velocity dependent collisional diffusion and velocity dependent (electrical) mobility respectively. The crux of the density-gradient driven heat-flow lies with the different v-dependencies of D' and μ'. For the usual Gaussian distribution, where $m = 2$, both $D' \propto v^4$ and $\mu' \propto v^4$, so that by the zero current condition (with j_x as the x-component $\mathbf{j}$), i.e.

$$j_x = -e\frac{4\pi}{3}\int_0^\infty f_x v^3\,\mathrm{d}v = 0, \tag{22}$$

the identical velocity dependence of D' and μ' implies that f_x must vanish for all v. In particular, since the integrand given by equation (21) has the same sign for all v when $m = 2$, it can never contrive to integrate up to zero unless $f_x = 0$, a condition which holds provided $eE_x = -T_\mathrm{e}\nabla \log n_\mathrm{e}$. Hence, with no finite flux f_x, isothermal, density-gradient driven heat-flow is prohibited when $m = 2$.

For $m > 2$ the velocity power for mobility μ' (i.e. $m+2 > 4$) is greater than the power for diffusion D' (i.e. 4), which means that high speed electrons in the tail of the distribution respond more to the electric field E_x than to collisional, diffusive forces down the density gradient[9]. Conversely, slow electrons, in the body of the distribution function near $v = 0$, preferentially move under the action of collisional diffusion. So the *overall* situation is of a flux of 'cold' electrons *down* the density gradient, balanced by a flux of 'hot' return electrons drawn by the electric field in the direction $-\mathbf{E}$ (i.e. *up* the density gradient, see equation (24) below). Thus, although the fluxes of cold-diffusion and hot-return electrons exactly balance (and therefore satisfy $j_x = 0$), the hot electrons carry more thermal energy $\propto v^2$, leading to a net energy flux $q_x = q_n \propto \partial n_\mathrm{e}/\partial x$ (as predicted from our fluid description in section 2.1.2 where we had $\mathbf{q}_\mathrm{n} \propto \nabla n_\mathrm{e}$).

Note that this situation is opposite to what happens in the classical case ($m = 2$) when there is a temperature gradient ($\nabla T_\mathrm{e} \neq \mathbf{0}$) and uniform density ($\nabla n_\mathrm{e} = \mathbf{0}$). Under these conditions the diffusive flux comprises hotter electrons than the return flux. Indeed, since $\mathbf{E} = -\nabla T/e$ for uniform density, we have that $\mathbf{f}_1$ is anti-parallel to ∇T for $v^2 > (5/2)v_\mathrm{T}^2$ and parallel when $v^2 < (5/2)v_\mathrm{T}^2$, i.e.

$$\mathbf{f}_1 = -\left\{\frac{v^4}{\nu'_\mathrm{ei}}\left[\left(\frac{v}{v_\mathrm{T}}\right)^2 - \frac{5}{2}\right]\nabla \log T_\mathrm{e}\right\} f_\mathrm{SG}(m=2). \tag{23}$$

In fact, for our original isothermal conditions, with $m \neq 2$, $\nabla T_\mathrm{e} = \mathbf{0}$ and $\nabla n_\mathrm{e} \neq \mathbf{0}$, one can calculate both the $\mathbf{E}$-field needed to yield zero-current, and the threshold speed separating the cold-diffusive and hot-return fluxes. The electric field turns out to satisfy

$$\frac{e\mathbf{E}}{m_\mathrm{e}} = -\frac{(\alpha_\mathrm{e}(m)v_\mathrm{T})^m}{m}\frac{\langle v^5\rangle_m}{\langle v^{3+m}\rangle_m}\nabla \log n_\mathrm{e}, \tag{24}$$

where $\langle v^p\rangle_m = \frac{4\pi}{n_\mathrm{e}}\int_0^\infty f_\mathrm{SG}(m)v^{p+2}\mathrm{d}v$ is a general velocity (magnitude) moment of the super-Gaussian distribution function for integer p, and is related to the Gamma function $\tilde{\Gamma}(x)$ (see

[9] This is because the tail of the super-Gaussian distribution function $f_\mathrm{SG}(m)$ drops more rapidly with v for $m > 2$, than for $m = 2$. More specifically, the balance between $\mathbf{E}$-field acceleration and frictional drag 'attempts' to shift the distribution function away from $v = 0$, and this shift leads to a larger change in $\mathbf{f}_1$ for the more rapidly diminishing $f_\mathrm{SG}(m > 2)$ than for the Gaussian $f_\mathrm{SG}(m = 2)$.

equation (1)) via

$$\langle v^p \rangle_m = v_{\mathrm{T}}^p \left(\frac{4\pi C(m) \alpha_{\mathrm{e}}^{p+3}}{m} \right) \tilde{\Gamma} \left(\frac{p+3}{m} \right). \tag{25}$$

This means that equation (21) can be expressed in the form

$$\frac{f_x}{f_{\mathrm{SG}}} = -D'_{\mathrm{a}} \frac{\partial n_{\mathrm{e}}}{\partial x} = -\left\{ \frac{v^4}{\nu'_{\mathrm{ei}}} \left[1 - \left(\frac{v}{\alpha_{\mathrm{e}} v_{\mathrm{T}}} \right)^{m-2} \frac{\tilde{\Gamma}(8/m)}{\tilde{\Gamma}(1+6/m)} \right] \right\} \frac{\partial \log n_{\mathrm{e}}}{\partial x}, \tag{26}$$

where $D'_{\mathrm{a}}(v)$ is an ambipolar diffusion coefficient for electrons of speed v. Hence, by inspecting the square brackets above, we can define a threshold velocity v_{cr} for the transition from collisional-diffusion dominated to **E**-field dominated electron motion, viz.

$$v_{\mathrm{cr}} = v_{\mathrm{T}} \alpha_{\mathrm{e}}(m) \left(\frac{\tilde{\Gamma}(8/m)}{\tilde{\Gamma}(1+6/m)} \right)^{1/(m-2)}. \tag{27}$$

For electron velocities $v > v_{\mathrm{cr}}$ the square-bracketed term in equation (26) is negative, in which case f_x is positive and represents electrons travelling in the direction of ∇n_{e}; whilst for $v < v_{\mathrm{cr}}$ the square-bracketed term is positive, meaning that these slower electrons move in the opposite direction. Values of the threshold velocity for $m = (2.1, 2.5, 3.0, 4.0, 5.0)$ are respectively $v_{\mathrm{cr}}/v_{\mathrm{T}} = (0.586, 0.776, 0.970, 1.24, 1.39)$ to three significant figures, and show a strong dependence on the super-Gaussian index for m just above 2. (Note: Although the analysis presented here is strictly valid when $\mathbf{B} = \mathbf{0}$, the general arguments also apply for weakly magnetized plasmas ($\chi \ll 1$).)

4. Inverse bremsstrahlung and the field-generating thermal instability

Our earlier summary in section 2.3 emphasizes the particular relevance of super-Gaussian transport theory when magnetic fields are weak (low χ), suggesting that it may have important consequences for the seeding and evolution of magnetic fields in otherwise unmagnetized conditions. For this reason, the following subsections are devoted to examining the consequences of the theory for the field-generating thermal instability mentioned in the introduction [24–28]; a context in which the Righi–Leduc heat-flow and the $\nabla T_{\mathrm{e}} \times \nabla n_{\mathrm{e}}$ field generation mechanism—both suppressed by IB—are essential. Indeed, because the equations of super-Gaussian transport predict a reduction in magnitude of effects responsible for both the growth *and* damping of unstable waves, such an analysis is particularly useful as a means of assessing the combined impact of the theory.

4.1. Perturbation analysis

In its basic form, for which hydrodynamical effects are neglected ($\partial n_{\mathrm{e}}/\partial t = 0$), the field-generating thermal instability is governed by the energy continuity equation (7) and the induction equation (11). Indeed, when combined with Ampére's law $\nabla \times \mathbf{B} = \mu_0 \mathbf{j}$, Ohm's law (equation (4)), and the heat-flow equation (5), these equations provide a complete description of the temporal variation in the principal quantities T_{e} and **B**. Note, however, that for most laser–plasmas of interest we can assume

$$\Lambda = \frac{\lambda_{\mathrm{T}}}{\delta} \gg 1, \quad \text{where } \delta = \frac{c}{\omega_{\mathrm{pe}}} \quad \text{and} \quad \omega_{\mathrm{pe}} = \left(\frac{n_{\mathrm{e}} e^2}{\epsilon_0 m_{\mathrm{e}}} \right)^{1/2} \tag{28}$$

are the collisionless-skin-depth and plasma frequency respectively, and c is the speed of light *in vacuo*, so that nonlinear first-order Ohmic heating terms arising $\mathbf{E}\cdot\mathbf{j}$ can be neglected [18].

For the perturbation analysis we suppose initially unmagnetized conditions: hence, the zeroth-order flux density is $\mathbf{B}=\mathbf{0}$ and for a general transport coefficient $\underline{\underline{\eta}}$ the zeroth-order component of $\eta_\perp$ is given by $\eta_\perp=\eta_\parallel$ (see section 2) [11–13]. In addition, we assert zeroth-order solutions for the temperature and number density $T_0\equiv T_0(x,t)$ and $n_0\equiv n_0(x)$ respectively, so that gradients in these quantities are along the x-axis of the system only. Consequently, providing we assume a laser heating profile parallel to the x-axis of the system, i.e. $\dot{U}_\mathrm{L}\equiv\dot{U}_\mathrm{L}(x)$, we can define zeroth-order temperature and density length-scales l_T and l_n such that

$$\frac{1}{l_\mathrm{T}}=\frac{1}{T_0}\frac{\partial T_0}{\partial x}\quad\text{and}\quad\frac{1}{l_n}=\frac{1}{n_0}\frac{\partial n_0}{\partial x}. \tag{29}$$

To the zeroth-order solutions we add wavelike perturbations with wavenumber k, frequency γ, and periodicity $\propto(\mathrm{i}ky+\gamma t)$, that is,

$$T_\mathrm{e}=T_0+\delta T\exp(\mathrm{i}ky+\gamma t)\quad\text{and}\quad\mathbf{B}=\delta B\exp(\mathrm{i}ky+\gamma t)\hat{\mathbf{z}}, \tag{30}$$

where δT and δB are complex, and $|\delta T|/T_0\ll 1$. Hence, after substituting these perturbed forms into the energy and induction equations, assuming the local conditions $|kl_{\mathrm{T},n}|\gg 1$ and $|\partial(l_{\mathrm{T},n}^{-1})/\partial x|\lesssim 1/l_{\mathrm{T},n}^2$, subtracting the zeroth-order solutions, and solving the resultant quadratic in k, we obtain the first-order dispersion relation [18]

$$\Gamma_\pm=\frac{1}{2}\left\{-\left[(D_\mathrm{T}+D_\mathrm{R})K^2-N\right]\pm\sqrt{\left[(D_\mathrm{T}+D_\mathrm{R})K^2-N\right]^2+4D_\mathrm{T}K^2\left[D_\mathrm{R}\left(K_\mathrm{G}^2-K^2\right)+N\right]}\right\}, \tag{31}$$

where N is an advection term defined in equation (33), and we have made use of an additional set of dimensionless quantities given by

$$\Gamma=\gamma\tau_\mathrm{T},\quad K=\lambda_\mathrm{T}k,\quad D_\mathrm{T}=\frac{c_\mathrm{B}}{3}\kappa'_\parallel,\quad D_\mathrm{R}=\frac{\alpha_\parallel^c}{c_\mathrm{B}\Lambda^2},\quad K_\mathrm{G}^2=\frac{C_\mathrm{E}C_\mathrm{I}}{D_\mathrm{T}D_\mathrm{R}},$$
$$C_\mathrm{E}=\frac{c_\mathrm{B}^2}{6L_\mathrm{T}}\left(\frac{\partial\kappa'_\wedge}{\partial\chi}+\frac{L_\mathrm{T}}{L_n}\frac{\partial\phi_\wedge^c}{\partial\chi}\right),\quad C_\mathrm{I}=\frac{\gamma_\parallel^c}{L_n}\quad\text{and}\quad L_{\mathrm{T},n}=\frac{l_{T,n}}{\lambda_\mathrm{T}}, \tag{32}$$

with super-Gaussian transformations $\kappa'_\parallel=\kappa_\parallel^c+\phi_\parallel^c$ and $\kappa'_\wedge=\kappa_\wedge^c+\phi_\wedge^c$. Notice here that D_T and D_R represent the dimensionless thermal and resistive diffusion coefficients respectively [29], while λ_T is the zeroth-order thermal mean-free-path and τ_T is the zeroth-order collision time. The 'field-generating source term' K_G^2 arises from coupling between the energy and induction equations, as described by the terms C_E and C_I respectively: C_E due to the Righi–Leduc and $\phi_\wedge^c$ heat-flows, and C_I due to field generation by $\nabla\delta T\times\nabla n_0$ (see figure 9). Finally, the advection term N accounts for both the conventional Nernst effect (see section 2.2.1), and the new isothermal 'anomalous Nernst' effect described in section 2.2.3; with $\beta'_\wedge=\beta_\wedge^c+\gamma_\wedge^c$ this term is defined by

$$N=N_\beta+N_\gamma,\quad\text{where } N_\beta=\lambda_\mathrm{T}^2\nu_\beta,\quad N_\gamma=\lambda_\mathrm{T}^2\nu_\gamma,$$
$$\nu_\beta=\frac{c_\mathrm{B}}{2}\frac{\partial\beta'_\wedge}{\partial\chi}\frac{1}{\tau_\mathrm{T}T_0}\frac{\partial}{\partial x}\left(\tau_\mathrm{T}\frac{\partial T_0}{\partial x}\right)\quad\text{and}\quad\nu_\gamma=\frac{c_\mathrm{B}}{2}\frac{\partial\gamma_\wedge^c}{\partial\chi}\frac{1}{\tau_\mathrm{T}n_0}\frac{\partial}{\partial x}\left(\tau_\mathrm{T}\frac{\partial n_0}{\partial x}\right). \tag{33}$$

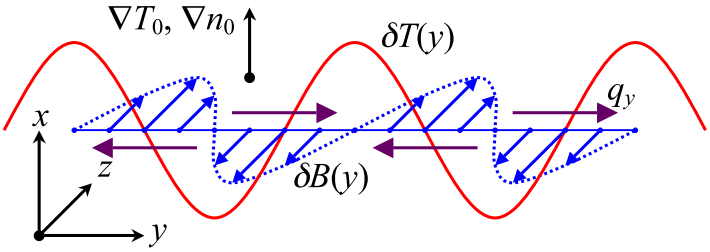

Figure 9. In the basic version of the field-generating thermal instability a temperature perturbation $\delta T(y)$ (red line) generates a magnetic field $\delta B(y)$ (blue arrows, dotted line) by the $\nabla\delta T \times \nabla n_0$ mechanism. Since the Righi–Leduc heat-flow from the bulk temperature gradient (purple arrows) is given by $q_y = -\kappa'_\wedge(\partial T_0/\partial x)(\delta B/|\delta B|)$, the alternating direction of $\delta B(y)$ periodically reverses q_y which then magnifies $\delta T(y)$ [18, 24, 25]. As described in equation (34), lateral transport of the field by terms in N can enhance this mechanism when advection is compressive ($N > 0$), but contributes to damping when rarefactive ($N < 0$).

Note that if we set the super-Gaussian power to $m = 2$, then we recover the dispersion relation derived by Hirao and Ogasawara [28], which itself reduces to that of Tidman and Shanny if $N = 0$ [24]. What we have called the *field-generating source term* K_G^2 therefore corresponds to instability arising from Tidman and Shanny's original mechanism [24, 25] (which we narrate in figure 9), while the advection term N can enhance instability by laterally compressing the magnetic field as a result of differential advection along bulk gradients. More formally, if the positive root is taken in equation (31), then instability prevails with growth-rate $\Gamma(K)$ for those values of K obeying

$$K < K_c = \left(K_G^2 + \frac{N}{D_R}\right)^{1/2}, \tag{34}$$

where K_c is the cut-off wave-number. Notice that since K has been assumed real, if $N \leqslant 0$, then we require $K_G^2 > 0$, which is only possible when the parallel gradient condition $L_T L_N > 0$ necessary for *positive* feedback between $\nabla\delta T \times \nabla n_0$ field generation and the Righi–Leduc heat-flow holds. If $L_T L_N < 0$, then $K_G^2 \leqslant 0$ and the interaction between $\nabla\delta T \times \nabla n_0$ field generation and the Righi–Leduc heat-flow results in *negative feedback damping* [18]; however, instability is still possible in this case whenever the advection term provides sufficient compression ($N > 0$) of the perturbation [28].

4.2. Peak growth-rates and interpretation of the advection mechanism

In addition to a cut-off wave-number, exact expressions may be found for both the peak wave-number K_M and growth-rate $\Gamma_M = \Gamma(K_M)$ by solving $(\partial\Gamma/\partial K)|_{K_M} = 0$ and then substituting for K_M in the dispersion relation. In this way we find [18]

$$K_M^4 = \begin{cases} \Gamma_M(\Gamma_M - N)/(D_T D_R) & \text{for} \quad K_G^2 > 0, \\ 0 & \text{for} \quad K_G^2 \leqslant 0, \end{cases} \tag{35}$$

where the peak growth-rate Γ_M is given by

$$\Gamma_M = \begin{cases} \dfrac{D_\mathrm{T} D_\mathrm{R}}{(D_\mathrm{T} - D_\mathrm{R})^2}[(D_\mathrm{T} K_\mathrm{c}^2 - N)^{1/2} - (D_\mathrm{R} K_\mathrm{c}^2 - N)^{1/2}]^2 & \text{for} \quad K_\mathrm{G}^2 > 0, \\ N & \text{for} \quad K_\mathrm{G}^2 \leqslant 0. \end{cases} \tag{36}$$

The seemingly unphysical possibility of a peak wave-number $K_M = 0$ reflects a rather curious feature of the dispersion relation: it ostensibly predicts unconditional instability with growth-rate $\Gamma = N$ in the limit $K \to 0$. Since such a limit clearly violates the local approximation $K_\mathrm{c} L_{\mathrm{T},n} \gg 1$, it implies an irregularity to the advection term which needs attention. As we saw in the previous subsection, when $K_\mathrm{G}^2 \leqslant 0$, lateral compression of the field is the sole mechanism by which the amplitude of the perturbation may be increased: since this compressive 'source' is lateral it is also independent on wave-number. Both negative feedback and diffusive damping are minimized at low K, so that amplification of the perturbation is maximized as $K \to 0$. This is an important aspect of the term in N because it tells us that advection does not contribute to instability in the usual way; it is simply a feature of advection that it can lead to exponential compression or rarefaction of the local magnetic field. Indeed, it is notable that in the dispersion relation (equation (31)) N does not contribute to coupling between the energy equation and induction equation in the same way as C_E and C_I, and so does not form part of a feedback loop. For this reason, even though it can enhance the impact of the traditional field-generating mechanism, it is perhaps inappropriate to refer to advection as actually driving instability *proper* [18][10].

4.3. Discussion

As a preliminary means of estimating the impact of super-Gaussian transport on actual instability growth-rates, we now evaluate Γ_M based on conditions found near to the wall of an inertial confinement fusion (ICF) hohlraum. This is an appropriate context for two reasons: firstly, the laser irradiation is of an intensity $\sim 2 \times 10^{15}\,\mathrm{W\,cm^{-2}}$ [2], for which IB is the main heating mechanism; and secondly, the high atomic number of gold ablating from the wall ($Z = 79$) makes the Lorentz approximation used to calculate the transport coefficients a good assumption [14]. Before proceeding, however, note that for most laser–plasma interactions of interest we can assume $\Lambda \gg 1$ (see equation (28)), in which case the peak growth-rates in equation (36) may be reduced to [18]

$$\Gamma_M = \begin{cases} D_\mathrm{R} K_\mathrm{c}^2 & \text{for} \quad K_\mathrm{G}^2 > 0, \\ N & \text{otherwise.} \end{cases} \tag{37}$$

Indeed, this simplified expression provides a convenient method for estimating growth-rates, and reduces the dimensionality of the problem to three length-scale coefficients b, a and λ_n defined by [18]

$$b = \frac{l_\mathrm{T}}{l_n}, \quad a = \frac{l_\mathrm{T}^2}{T_0}\frac{\partial^2 T_0}{\partial x^2} \quad \text{and} \quad \lambda_n = \left(\frac{l_n}{n_0}\frac{\partial^2 n_0}{\partial x^2}\right)^{-1}. \tag{38}$$

[10] It is something of a moot point whether or not consistent application of the local approximation should exclude N from the first-order dispersion relation at the outset [18]. Nevertheless, since Hirao and Ogasawara [28] keep an advection term in their relation, we shall retain ours.

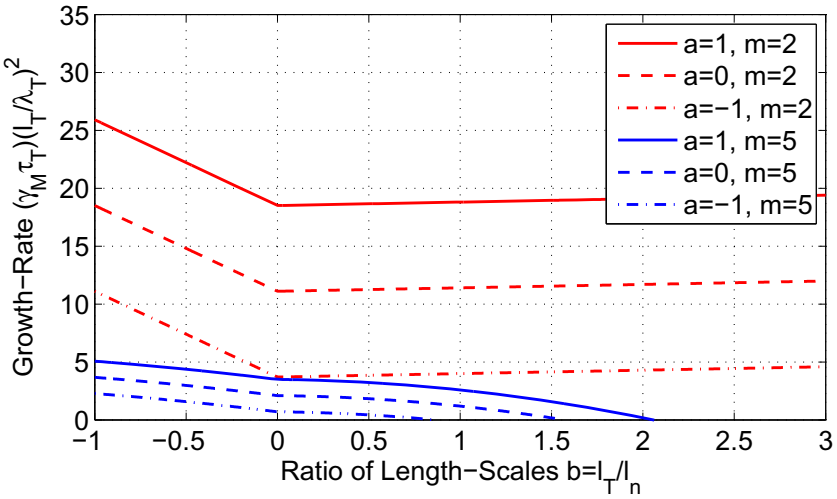

Figure 10. The value of $\gamma_M \tau_T (l_T/\lambda_T)^2$ plotted against $b = l_T/l_n$ for three values of $a = (l_T^2/T_0)(\partial^2 T_0/\partial x^2)$, and the super-Gaussian powers $m = 2$ and 5. Here the plots for $b \leqslant 0$ and $b > 0$ use $\gamma_M \tau_T = N$ and $\gamma_M \tau_T = D_R K_c^2$ respectively, as appropriate to equation (37), and the sign of $b/|b| = K_G^2/|K_G^2|$. Notice the strong suppression of the peak growth-rate for the Langdon distribution (blue curves, $m = 5$) when compared to the classical transport case (red curves, $m = 2$).

Temperature and density profiles along the ray-path of an outer hohlraum heating beam are given in [2], and using these data it is possible to estimate the length-scales close to the hohlraum wall: avoiding stationary points, typical values are $a \in [-1, 1]$ and $b \in [-1, 3]$, with $l_n/\lambda_n \approx 2$ [18]. Peak growth-rates evaluated in this range are given in figure 10 (using the dimensional lower-case notation $\gamma_M = \Gamma_M/\tau_T$ and $l_T = L_T \lambda_T$) from which, with $a = 0$, $b = 1$ and $m = 2$, we find

$$\Gamma_M = \gamma_M \tau_T \approx 10\,(\lambda_T/l_T)^2\,. \tag{39}$$

For the near-wall conditions described, where $T_e \sim 4.5\,\mathrm{keV}$, $n_e \sim 10^{21}\,\mathrm{cm}^{-3}$, $\lambda_T \sim 10\,\mu\mathrm{m}$, $\tau_T \sim 0.25\,\mathrm{ps}$ and $l_T \sim 3\,\mathrm{mm}$, this equation predicts $\gamma_M \sim 0.45\,\mathrm{ns}^{-1}$, suggesting that the field-generating thermal instability can undergo over six e-foldings during a 13.5 ns ignition pulse [2]. However, combining the normalized quiver velocity formula (equation (3)) with the formula for m (equation (2)), and using appropriate values for the laser intensity and wavelength of $I_l \sim 2 \times 10^{15}\,\mathrm{W\,cm}^{-2}$ and $\lambda_l = 351\,\mathrm{nm}$ respectively [2], we find that the super-Gaussian power near the hohlraum wall is $m \sim 3$, meaning our estimates should be compared with others based on larger values of m.[11]

The ratio of peak growth-rates $\gamma_M(m = 3)/\gamma_M(m = 2)$ is plotted in figure 11 (top), a comparison indicating reduction in the field-generating thermal instability growth-rate by more than ∼60% when super-Gaussian transport theory is employed as the basis description. Combining this result with our calculation from the previous paragraph, we find that the growth-rate for the $m = 3$ case when $b = 1$ and $a = 0$ is $\gamma_M \sim 0.2\,\mathrm{ns}^{-1}$. Over a 13.5 ns time-scale we

[11] The estimates in this paragraph have been made using the formulae given in appendix B, and assuming the following parameters: $n_e \sim 10^{21}\,\mathrm{cm}^{-3}$, $T_e \sim 4$–$5\,\mathrm{keV}$, $Z \sim 79$ and $\log \Lambda_{ei} \sim 6$.

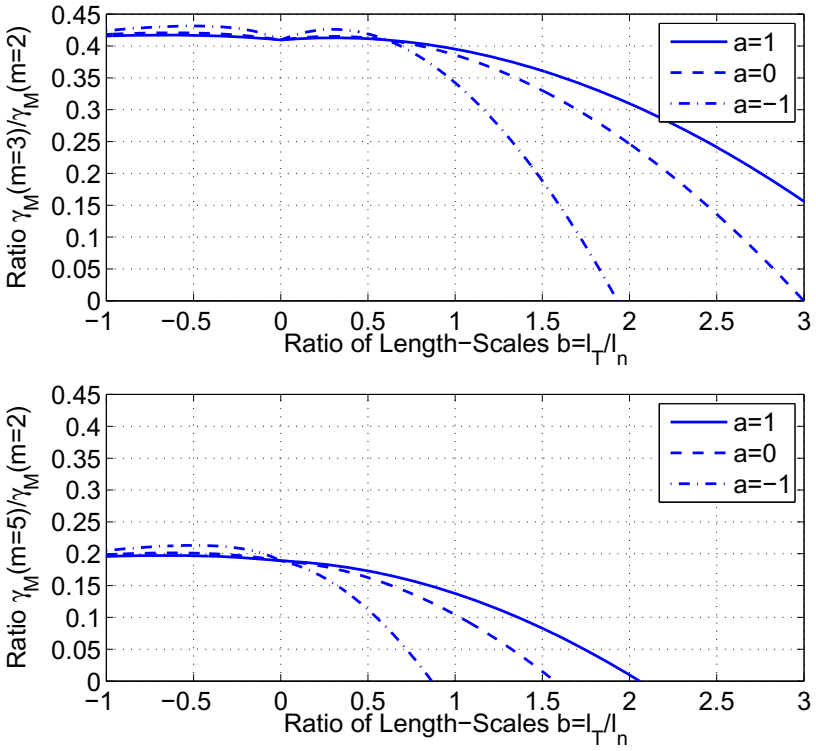

Figure 11. Top: the ratio $\gamma_M(m=3)/\gamma_M(m=2)$ plotted as a function of $b = l_T/l_n$ for different values of $a = (l_T^2/T_0)(\partial^2 T_0/\partial x^2)$. Bottom: the same ratio, but for stronger IB heating, i.e. $\gamma_M(m=5.0)/\gamma_M(m=2)$ plotted as a function of b for different values of a. In both cases, the curves for $b \leqslant 0$ and $b > 0$ correspond to those in figure 10. Note suppression of the field-generating instability by more than ∼60% when $m = 3.0$ (top), exceeding ∼80% when $m = 5.0$ (bottom).

thus expect the instability to undergo less than two-and-a-half e-foldings, rendering questionable its significance for the hohlraum conditions described; for example, the reduced number of e-foldings corresponds in principle to only 3% of the growth in perturbation amplitude relative to the classical transport case ($e^{2.5}/e^6 \approx 0.03$). Increasing the strength of IB heating may therefore help to quench the production of magnetic field in ICF fusion schemes.

Indeed, as shown in figure 10, super-Gaussian effects reduce the impact of the instability in two ways: firstly, they suppress the absolute growth-rate; and secondly, they restrict the range of b over which the instability remains active. Naturally, the overall reduction in the growth-rate is a consequence of the way in which transport terms are suppressed in the super-Gaussian theory, as we discussed in section 2. The restricted range of b, however, results from competition between the traditional (classical) phenomena and the new super-Gaussian effects: (i) conventional Nernst advection $\mathbf{v}_N \propto \nabla T_e$ as opposed to the new 'anomalous Nernst' effect $\mathbf{v}_\gamma \propto \nabla n_e$; and (ii) Righi–Leduc heat-flow as opposed to the cross-field ($\phi^c_\wedge$) part of the new heat-flow $\mathbf{q}_\phi \propto \underline{\underline{\phi^c}} \cdot \nabla n_e$. This aspect of our analysis is most clear in the heat-flow terms; indeed, from the definition of $K_G^2 \propto C_E C_I$, we see that the field-generating source term becomes negative—a

source of damping rather than instability—for those value of b exceeding the upper limit

$$b_{\max.} = \left(\frac{\partial \kappa'_{\wedge}}{\partial \chi}\right) \left|\frac{\partial \phi^{c}_{\wedge}}{\partial \chi}\right|^{-1} \approx \begin{cases} 10 & \text{for} \quad m = 3, \\ 5 & \text{for} \quad m = 5. \end{cases} \tag{40}$$

This result is consistent with the observation that even greater suppression of the instability ($\gtrsim 80\%$) can be achieved for further increases to the strength of IB heating, i.e. $m \to 5$ (see figure 11, bottom). Note that there is no upper limit $b_{\max.}$ for positive values of K_{G}^2 when classical transport conditions apply ($m = 2$).

It should be observed, however, that ablation from the wall is also likely to impact on the growth of perturbations, and may help to stabilize the instability (by convecting material from the region of field generation), or even—under some conditions—enhance it (in a fashion similar to the Nernst compression described in section 4.2). Ideally, these potential losses (or gains) should be accounted for when making future estimates.

5. Conclusions

This article has been concerned with furthering understanding of super-Gaussian transport theory [14]: a version of classical transport theory [11–13] valid under conditions for which strong IB heating distorts the electron distribution function to a super-Gaussian, i.e. $f_0 \propto \exp(-[v/\alpha_{\mathrm{e}} v_{\mathrm{T}}]^m)$, where $m \in [2, 5]$ and α_{e} is a function of m. Broadly speaking, our discussion has been divided along two themes: firstly, super-Gaussian modifications to classical transport; and secondly, IB quenching of the field-generating thermal instability [24, 25].

In the first part (section 2) we showed that the 'new' super-Gaussian coefficients resulting from IB (those absent in the equations of classical transport) both substantially suppress traditional transport effects, and give rise to new phenomena: features which we motivated physically in terms of the underlying distribution function. In particular, we demonstrated a reduction in the diffusive and Righi–Leduc heat-flows by as much as $\sim$80 and $\sim$90% respectively, a consequent lowering of the Nernst advection velocity in accordance with the diffusive heat-flow ($\sim$80%), and suppression of the $\nabla T_{\mathrm{e}} \times \nabla n_{\mathrm{e}}$ magnetic field generation mechanism by up to 30%. The newly introduced phenomena both relate to density gradients: firstly, isothermal heat-flow $\mathbf{q}_{\mathrm{n}} \propto \nabla n_{\mathrm{e}}$; and secondly, an (associated) isothermal *anomalous Nernst effect*, which carries field with $\mathbf{q}_{\mathrm{n}}$. Bulk advection may be very important for determining the saturation field following $\nabla T_{\mathrm{e}} \times \nabla n_{\mathrm{e}}$ generation and effective instability growth rates (due to spatial dissipation).

The strong suppression of thermal transport in the new theory is of particular significance, and may be especially pronounced during initial stages of heating when the ratio of the electron quiver velocity $v_{\mathrm{osc.}}$ to the thermal velocity v_{T} is greatest, i.e. when IB is strongest ($v_{\mathrm{osc.}}/v_{\mathrm{T}} \gg 1$), and the super-Gaussian index m largest. One potential consequence of such reduction is enhanced formation of localized hotspots, which would impact on hydrodynamic forces due to the steepening of temperature gradients. Indeed, hotspots may be relevant to a number of experimental conditions, particularly direct drive ICF where the fuel ablator is heated directly by IB, and drive uniformity is of primary concern [43]. Isothermal effects predicted by our theory might also be important in this context, particularly in the coronal plasma just beyond critical density, where standard hydrodynamic modelling predicts density gradients, but a relatively uniform temperature. By advecting magnetic field via our *anomalous Nernst*

effect, the new $\mathbf{q}_n \propto \nabla n_e$ heat-flow might be expected to contribute significantly to both thermal profiles and **B**-field evolution is this region.

However, it should be noted that the comparisons between classical and super-Gaussian theory made here are based on values for the coefficients calculated in the Lorentz approximation ($Z \to \infty$), and should ideally be repeated for a range of Z. One method of doing this would be to incorporate electron–electron collisions in the derivation of the transport coefficients (see appendix C), and to recalculate them for different atomic numbers. Such an approach would be essentially identical to that of Epperlein and Haines [13], who derived *classical* transport coefficients for $Z \neq \infty$ plasmas, but would use super-Gaussians for the underlying distribution function f_0 (see appendix C). In this way, the impact of the super-Gaussian theory could be assessed as we have done here for generalized values of Z. This kind of theoretical development warrants further examination, and is recommended as future work.

Having discussed the new super-Gaussian phenomena from a fluid perspective in section 2, we demonstrated their validity kinetically using our VFP code IMPACT in section 3. Two scenarios were considered: in the first (section 3.1), we employed an artificial electron–electron collision operator (see appendix A.1) to artificially relax f_0 to a super-Gaussian of chosen power m; while in the second (section 3.2), we used the more realistic Langdon IB operator, which naturally forces $f_0 \to f_{SG}$ [16], to heat a density profile.

The origin of density-gradient driven heat-flow $\mathbf{q}_n \propto \nabla n_e$ for super-Gaussian distributions with $m > 2$ has been shown to arise from different velocity dependences in the collisional diffusion and electrical mobility coefficients, D' and μ' respectively, which drive electron fluxes (section 3.3). When $m = 2$, both coefficients scale as v^4, which precludes overall energy transfer since the necessary electron flux would lead to a net electrical current (and violation of quasi-neutrality). If $m \neq 2$, then this complete cancellation is broken, and results in a diffusive flow of 'cold' electrons down the density gradient balanced by a return flux of 'hot' electrons drawn by the electric field, a configuration which yields net thermal transport in the direction ∇n_e. This emergence of density driven heat-flow is in keeping with other non-intuitive phenomena exhibited by plasmas far from thermodynamic equilibrium (e.g. the heat-flow 'non-parallel' to $-\nabla T_e$ observed by Rickard *et al* [41]). Recent papers addressing the kinetic analysis of unmagnetized plasmas with super-Gaussian distribution functions support our findings [22, 42]; indeed, though these articles do not discuss the physical basis for such effects, they also demonstrate both heat-flow in the direction ∇n_e [22] and suppressed thermal conduction along $-\nabla T_e$ [22, 42].

Modifications to classical transport theory introduced by super-Gaussian distortions are most substantial at low Hall parameter ($\chi \lesssim 10^{-2}$, see figures 3 and 4), implying that the theory is especially relevant to describing the generation and evolution of magnetic fields in otherwise unmagnetized plasmas. Consequently, in section 4 we examined the impact of super-Gaussian transport on the field-generating thermal instability, a context of pronounced feedback in which we expect combined effects to be most apparent [24, 25]. Initial estimates based on ICF hohlraum conditions [2] suggest that super-Gaussian distortion of the distribution function to $m \sim 3$ can limit the range of instability and suppress growth-rates by more than $\sim$60% relative to the classical transport case ($m = 2$). Further estimates with super-Gaussian power $m = 5$ indicate suppression in excess of $\sim$80%; this is presumably good news for ICF fusion experiments, since by increasing the strength of IB heating it would appear possible to inhibit the spontaneous generation of large magnetic fields. However, these preliminary estimates could be

improved in future studies by developing a more comprehensive analysis inclusive of potential convective effects.

Though hydrodynamical effects were neglected in our analysis, previous studies of the field-generating thermal instability suggest that plasma motion will not significantly alter the estimates given here, and that the fractional suppression of growth-rates will remain largely similar [27, 28]. However, the super-Gaussian transport equations assume $\nabla m = \mathbf{0}$ in their present form, and require additional generalization if they are to be of more universal validity, and, indeed, possible augmentation with an hydrodynamic equation to determine the spatial evolution of m itself. Preliminary work based on hohlraum gas-fill conditions suggests that taking $\nabla m \neq \mathbf{0}$ would have a negligible impact on the calculations given here [44]; nevertheless, Huo *et al* [22] predict that m-gradients may be important deeper in the hohlraum ablation layer, and the extension of Ohm's law (equation (4)) and the heat-flow equation (equation (5)), to incorporate magnetized terms in ∇m, should therefore form part of future theoretical analyses. Further research is also necessary to better assess the impact of super-Gaussian effects arising from IB when compared to other kinetic phenomena, such as non-local heat-flow. Indeed, while ongoing studies suggest that phenomena associated with IB heating persist alongside mild non-local effects, and that super-Gaussian theory provides valuable supplementary insight when interpreting kinetic results, more work is needed to fully distinguish between the two [14, 18, 29].

Acknowledgments

JJB acknowledges support from a Leverhulme Trust Grant (Tipping Points, Institute of Hazard, Risk, and Resilience, University of Durham), and a United Kingdom Engineering and Physical Sciences Research Council (E.P.S.R.C.) Doctoral Training Grant (no. EP/P502500/1). This work was made possible by use of the Imperial College High Performance Computing Service.

Appendix A. Further background to the kinetic simulations

In IMPACT the electron distribution function $f \equiv f(\mathbf{r}, \mathbf{v}, t)$, which takes as its arguments both spatial position $\mathbf{r}$ and electron velocity $\mathbf{v}$ vectors, is approximated as the sum of isotropic $f_0(\mathbf{r}, v, t)$ and anisotropic $\mathbf{f}_1(\mathbf{r}, v, t)$ components, such that $f = f_0 + \mathbf{f}_1 \cdot \mathbf{v}/v$, with $v = |\mathbf{v}|$ [23]. Macroscopic plasma quantities, such as temperature and heat-flow, may then be calculated by evolving f and taking suitable velocity moments of f_0 and $\mathbf{f}_1$ [38, 39]. In particular, IMPACT solves for f in terms of the VFP equation expanded as the so-called f_0 and $\mathbf{f}_1$-equations [38, 39], respectively

$$\frac{\partial f_0}{\partial t} - \frac{v}{3}\nabla \cdot \mathbf{f}_1 - \frac{e/m_\mathrm{e}}{3v^2}\frac{\partial}{\partial v}(v^2 \mathbf{E} \cdot \mathbf{f}_1) = \left[\frac{\partial f_0}{\partial t}\right]_\mathrm{C} + \left[\frac{\partial f_0}{\partial t}\right]_\mathrm{H} \tag{A.1}$$

$$\text{and} \quad \frac{\partial \mathbf{f}_1}{\partial t} + v\nabla f_0 - \frac{e\mathbf{E}}{m_\mathrm{e}}\frac{\partial f_0}{\partial v} - \frac{e}{m_\mathrm{e}}(\mathbf{B} \times \mathbf{f}_1) = \left[\frac{\partial \mathbf{f}_1}{\partial t}\right]_\mathrm{C}, \tag{A.2}$$

where $[\partial f_0/\partial t]_\mathrm{C}$ is the electron–electron collision operator, $[\partial \mathbf{f}_1/\partial t]_\mathrm{C}$ is the $\mathbf{f}_1$ collision operator, and $[\partial f_0/\partial t]_\mathrm{H}$ is a source of external (laser) heating. Hydrodynamic effects (not shown above) and electron inertia ($\partial \mathbf{f}_1/\partial t = \mathbf{0}$) feature in IMPACT, but are neglected here: the former given that hydrodynamic timescales broadly exceed those associated with electron transport; and the latter

both for consistency with the super-Gaussian Ohm's law of equation (4), and because in practice electron inertia tends to be unimportant unless time and length-scales are comparatively short (of order the Debye length $\frac{1}{\sqrt{2}}(v_T/\omega_{pe})$ and inverse plasma frequency $1/\omega_{pe}$ respectively).

Our simulations in section 3 are based on exploiting the f_0-equation, and we use it to drive the isotropic part of the distribution towards a super-Gaussian in two ways: firstly (section 3.1), via artificial collisional relaxation (employing a modified collision operator); and secondly (section 3.2), by more realistic continuous IB heating. For reference purposes, both of these processes are described in the following subsections.

A.1. Artificial distortion by generalized electron–electron collisions

For our verification simulations in section 3.1, the usual IMPACT electron–electron collision operator [23] is modified to the form

$$\left[\frac{\partial f_0}{\partial t}\right]_C = \frac{\nu'_{ee}}{v^2}\frac{\partial}{\partial v}\left[C_l(v, f_0)\, f_0 + D_{m,l}(v, f_0)\frac{\partial f_0}{\partial v}\right], \quad \text{where} \tag{A.3}$$

$$C_l = 4\pi\int_0^v u^l f_0(u)\mathrm{d}u \quad \text{and} \quad D_{m,l} = \frac{4\pi}{v^{m-1}}\int_0^v u^l\left\{\int_u^\infty f_0(w)w^{m-1}\mathrm{d}w\right\}\mathrm{d}u$$

are (artificially) generalized *Rosenbluth coefficients* [45], designed to make the electron–electron collision operator relax the isotropic part of the distribution function f_0 to a super-Gaussian $f_{SG}(m)$ with selectable m. Here l is a free index for experimentation, u and w are dummy speed variables, and $\nu'_{ee} = [(e^2/\epsilon_o m_e)^2/4\pi]\log\Lambda_{ee}$, with Λ_{ee} as the Coulomb logarithm for electron–electron scattering. Taking $m = 2$ and $l = 2$, equation (A.3) reduces to the usual collision operator with standard (physical) Rosenbluth coefficients, and for which collisions make f_0 tend to a Gaussian $f_0 \to f_{SG}(2)$.

It can be shown that inserting $f_0 = f_{SG}(m)$ into the generalized Rosenbluth coefficients makes the collision operator vanish, that is,

$$\left[\frac{\partial f_0}{\partial t}\right]_C = \frac{\nu'_{ee}}{v^2}\frac{\partial}{\partial v}\left[C_l(v, f_{SG})\, f_{SG} + D_{m,l}(v, f_{SG})\frac{\partial f_{SG}}{\partial v}\right] = 0 \tag{A.4}$$

as required for equilibrium. In particular, for steady state with $\partial f_0/\partial t = 0$, etc (see equation (A.1)), the collision operator $[\partial f_0/\partial t]_C = 0$ yields a linear ordinary differential equation $0 = C_k(v) f_{SG} + D_{m,k}(v)\partial f_{SG}/\partial v$, which has standard solution

$$f_{SG} \propto \exp\left[-\int \left(C_l/D_{m,l}\right)\mathrm{d}v\right] \quad \Rightarrow \quad f_{SG} \propto \exp\left[-(v/\alpha_e v_T)^m\right],$$

$$\text{since} \quad D_{m,l} = \frac{(\alpha_e v_T)^m}{(m v^{m-1})}C_l \quad \Rightarrow \quad \int (C_l/D_{m,l})\mathrm{d}v = (v/\alpha_e v_T)^m. \tag{A.5}$$

The numerical implementation of C_l and $D_{m,l}$ is beyond the scope of this paper; for present purposes we simply observe that by using the generalized collision operator with a chosen super-Gaussian power m, IMPACT does indeed relax to $f_{SG}(m)$ whilst perfectly conserving electron density, and with virtually perfect conservation of thermal energy. (Note: For the idealized VFP simulations described in section 3.1 we take $l = 2$ throughout.)

A.2. Realistic distortion by continual inverse bremsstrahlung heating

Distortion of the electron distribution towards a super-Gaussian by IB is well documented [14, 16, 17], and in our more realistic plasma heating simulations (section 3.2) $f_0 \to f_{\rm SG}$ is therefore achieved simply by employing IMPACT's usual Langdon IB operator [16]:

$$\left[\frac{\partial f_0}{\partial t}\right]_{\rm H} \to \left(\frac{\partial f_0}{\partial t}\right)_{\rm IB} = \nu'_{\rm ei}\frac{v^2_{\rm osc.}}{v^2}\frac{\partial}{\partial v}\left(\frac{g(v)}{6v}\frac{\partial f_0}{\partial v}\right), \tag{A.6}$$

where $\nu'_{\rm ei} = [(e^2/\epsilon_o m_{\rm e})^2/4\pi]Z^2 n_{\rm i}\log\Lambda_{\rm ei}$ is the velocity independent part of the electron–ion collisional scattering frequency $\nu_{\rm ei}(v) = \nu'_{\rm ei}/v^3$, and $v_{\rm osc.}$ is the quiver velocity given in equation (3). In significantly under-dense plasmas $g(v)$ may be expressed as $g(v) = [1 + (\omega_{\rm l}/\nu_{\rm ei}(v))^{-2}]^{-1} \to 1$, where $\omega_{\rm l}$ is the laser angular frequency, since $\omega_{\rm l} \ll \nu_{\rm ei}$ (this approximation typically holds for all parts of the electron distribution function except the very coldest, most collisional electrons with $v \ll v_{\rm T}$).

Inverse bremsstralung augments electron–electron collisions acting on f_0 (see equation (A.1)), so its implementation in IMPACT is straightforward: $(\partial f_0/\partial t)_{\rm IB}$ essentially takes the form of a diffusive operator, and the relevant Rosenbluth coefficient is modified accordingly, that is,

$$D(v) \to D(v) + D_{\rm IB}(v), \quad \text{with } D_{\rm IB}(v) = \nu'_{\rm ei}\frac{v^2_{\rm osc.}g(v)}{6v}, \tag{A.7}$$

where for the continual IB heating simulations in section 3.2 we use the standard (physical) Rosenbluth coefficients, i.e. $D(v) = D_{m=2,l=2}(v)$ (see equation (A.3)).

Setting $g(v) = 1$ (as we do in section 3.2), the IB heating rate is found by taking the energy moment of equation (A.6), viz.

$$\left(\frac{\partial T_{\rm e}}{\partial t}\right)_{\rm IB} = \frac{8\pi}{3n_{\rm e}}\int_0^\infty v^2\left(\frac{\partial f_0}{\partial t}\right)_{\rm IB}v^2{\rm d}v = \left[\frac{4}{9\sqrt{\pi}}\frac{m_{\rm e}v^2_{\rm osc.}}{\tau_{\rm T}}\right], \tag{A.8}$$

where the final square-bracketed form applies only for the Gaussian distribution $f_0 = f_{\rm SG}(2)$, and we have neglected hydrodynamic effects by assuming constant density.

Appendix B. Useful formulae for plasma parameters

With $T_{\rm e}$ and $n_{\rm e}$ measured in keV and cm^{-3} respectively, the following formulae provide a convenient means for calculating plasma parameters and conditions in sections 3 and 4 [18]:

- *Thermal mean-free-path* (with $\lambda_{\rm T}$ measured in microns)

$$\left(\frac{\lambda_{\rm T}}{\mu{\rm m}}\right) \approx 3\left(\frac{\log\Lambda_{\rm ei}}{5}\right)^{-1}\left(\frac{Z}{10}\right)^{-1}\left(\frac{n_{\rm e}}{10^{21}\,{\rm cm}^{-3}}\right)^{-1}\left(\frac{T_{\rm e}}{\rm keV}\right)^2. \tag{B.1}$$

- *Thermal electron–ion collision time* (with $\tau_{\rm T}$ measured in picoseconds)

$$\left(\frac{\tau_{\rm T}}{\rm ps}\right) \approx \frac{1}{6}\left(\frac{\log\Lambda_{\rm ei}}{5}\right)^{-1}\left(\frac{Z}{10}\right)^{-1}\left(\frac{n_{\rm e}}{10^{21}\,{\rm cm}^{-3}}\right)^{-1}\left(\frac{T_{\rm e}}{\rm keV}\right)^{3/2}. \tag{B.2}$$

- *Hall parameter* χ *and thermal Larmor radius* $r_{\rm L}$ (with $|\mathbf{B}|$ measured in tesla)

$$\chi = \frac{3\sqrt{\pi}}{4}\left(\frac{\lambda_{\rm T}}{\mu{\rm m}}\right)\left(\frac{\mu{\rm m}}{r_{\rm L}}\right) \approx \frac{1}{4}\left(\frac{\tau_{\rm T}}{\rm ps}\right)\left(\frac{|\mathbf{B}|}{T}\right). \tag{B.3}$$

- *Coulomb logarithm*

$$\log \Lambda_{ei} \approx 6.9 - \log\left(\frac{Z}{10}\right) + \frac{3}{2}\log\left(\frac{T_e}{\text{keV}}\right) - \frac{1}{2}\log\left(\frac{n_e}{10^{21}\,\text{cm}^{-3}}\right). \tag{B.4}$$

- *Ratio of mean-free-path λ_T to collisionless skin-depth δ*

$$\Lambda = \frac{\lambda_T}{\delta} \approx \frac{1}{5.48\times 10^{-2}}\left(\frac{n_e}{10^{21}\,\text{cm}^{-3}}\right)^{-1/2}\left(\frac{Z}{10}\right)^{-1}\left(\frac{\log\Lambda_{ei}}{5}\right)^{-1}\left(\frac{T_e}{\text{keV}}\right)^{2}. \tag{B.5}$$

Appendix C. Background to the super-Gaussian transport equations

Though Dum [15] developed the first transport model applicable to plasmas with super-Gaussian distribution functions, it is the version of the theory developed by Ridgers *et al* [14], who additionally calculated polynomial fits to the transport coefficients for a range of m, that forms the main background to the work presented here. For the purpose of completeness, this latter approach is outlined below.

Ridgers' derivation closely follows the work of Epperlein [12], taking as its starting point the distribution function f expanded in Cartesian tensors, that is, $f = f_0 + \mathbf{f}_1 \cdot \mathbf{v}/v$, where f_0 and $\mathbf{f}_1$ are its isotropic and anisotropic components respectively (see appendix A), and are functions of velocity magnitude only. In *classical* transport theory f_0 is taken to be a Gaussian, whereas in Ridgers' derivation a super-Gaussian is used, i.e.

$$f_0 = f_{SG}(v) = C(m)\frac{n_e}{v_T^3}\exp\left[-\left(\frac{v}{\alpha_e v_T}\right)^m\right], \quad \text{with } m \in [2,5], \tag{C.1}$$

where $C(m)$ and $\alpha_e(m)$ were defined in equation (1) (see section 1).

The transport equations themselves are calculated by taking velocity moments of the $\mathbf{f}_1$-equation, which Epperlein and Ridgers employ in the form (cf appendix A)

$$v\nabla f_0 - \frac{e\mathbf{E}}{m_e}\frac{\partial f_0}{\partial v} - \frac{e}{m_e}(\mathbf{B}\times\mathbf{f}_1) = \nu_{ei}\mathbf{f}_1, \tag{C.2}$$

where $\nu_{ei}(v) = \left(\left[Ze^2/\epsilon_0 m_e\right]^2 n_i \log\Lambda_{ei}/4\pi v^3\right)$ is the electron–ion collision frequency for electrons travelling at speed v, and we have made use of the *Lorentz approximation*, that is, electron–electron collisions are neglected when compared to electron–ion collisions[12]. Indeed, by substituting $f_0 = f_{SG}$ from equation (C.1) into equation (C.2), and then taking both current $\mathbf{j} = -\frac{4\pi}{3}e\int_0^\infty v^3\mathbf{f}_1\,\mathrm{d}v$ and heat-flow $\mathbf{q} = \frac{2\pi}{3}m_e\int_0^\infty v^5\mathbf{f}_1\,\mathrm{d}v$ moments of the result, one arrives at expressions for Ohm's law (equation (4)) and the heat-flow equation (equation (5)) comprising tensor terms of the form (see section 2)

$$\underline{\underline{\eta}}\cdot\mathbf{s} = \eta_\parallel\mathbf{b}(\mathbf{b}\cdot\mathbf{s}) + \eta_\perp\mathbf{b}\times(\mathbf{s}\times\mathbf{b}) + \eta_\wedge\mathbf{b}\times\mathbf{s}, \quad \text{with } \mathbf{b} = \frac{\mathbf{B}}{|\mathbf{B}|}, \tag{C.3}$$

$$\eta \in \{\alpha^c, \beta^c, \kappa^c, \gamma^c, \psi^c, \phi^c\}, \quad \text{and} \quad \mathbf{s} \in \{\nabla P_e, \mathbf{j}, \nabla T_e\}. \tag{C.4}$$

In Ridgers' super-Gaussian theory, the $\eta_\parallel$, $\eta_\perp$ and $\eta_\wedge$ type tensor components are defined by combinations of integral moments of f_{SG} that may be evaluated numerically for given m and

[12] Electron–ion collisions dominate angular scattering at high Z. The electron inertia term $\partial\mathbf{f}_1/\partial t$ is also neglected on the basis that we do not wish to resolve timescales of order $1/\omega_{pe}$ (see appendix A).

χ [14], and it is these numerically obtained coefficients which form the basis of our comparative work in sections 2 and 4.

It is worth noting that a more general super-Gaussian theory could be derived along similar lines to Epperlein and Haines's classical theory [13] by retaining electron–electron collisions in the $\mathbf{f}_1$-equation. In this way, the Lorentz approximation is avoided, and the super-Gaussian coefficients can be recalculated to more accurately describe transport at low atomic number Z. We recommend such a procedure as future work in section 5.

References

[1] Glenzer S H *et al* 1999 *Phys. Plasmas* **6** 2117–28
[2] Lindl J *et al* 2004 *Phys. Plasmas* **11** 339–491
[3] Nilson P M *et al* 2006 *Phys. Rev. Lett.* **97** 255001
[4] Frolov B *et al* 2006 *New J. Phys.* **8** 56
[5] Froula D H *et al* 2007 *Phys. Rev. Lett.* **98** 135001
[6] Li C K *et al* 2007 *Phys. Rev. Lett.* **99** 015001
[7] Li C K *et al* 2007 *Phys. Rev. Lett.* **99** 055001
[8] Schurtz G *et al* 2007 *Phys. Rev. Lett.* **98** 095002
[9] Froula D H *et al* 2009 *Plasma Phys. Control. Fusion* **51** 024009
[10] Li C K *et al* 2009 *Phys. Rev.* E **80** 016407
[11] Braginskii S I 1965 Transport processes in a plasma *Rev. Plasma Phys.* **1** 205
[12] Epperlein E M 1984 *J. Phys. D: Appl. Phys.* **17** 1823–7
[13] Epperlein E M and Haines M G 1986 *Phys. Fluids* **29** 1029–41
[14] Ridgers C P *et al* 2008 *Phys. Plasmas* **15** 092311
[15] Dum C T 1978 *Phys. Fluids* **21** 956–69
[16] Bruce A Langdon 1980 *Phys. Rev. Lett.* **44** 575–9
[17] Matte J P *et al* 1988 *Plasma Phys. Control. Fusion* **30** 1665–85
[18] Bissell J J 2011 Magnetised transport and instability in laser produced plasmas *PhD Thesis* Imperial College London
[19] Kingham R J 2004 Magnetic fields in gas-filled hohlraums *Technical Report* Imperial College London
[20] Haines M G 1986 *Plasma Phys. Control. Fusion* **28** 1705–16
[21] Zhu S P and Gu P J 1999 *Chin. Phys. Lett.* **16** 520–2
[22] Huo W Y *et al* 2012 *Phys. Plasmas* **19** 012313
[23] Kingham R J and Bell A R 2004 *J. Comput. Phys.* **194** 1–34
[24] Tidman D A and Shanny R A 1974 *Phys. Fluids* **17** 1207–10
[25] Bol'shov L A *et al* 1974 *JETP Lett.* **19** 168–70
[26] Brownell J H 1979 *Comments Plasma Phys. Control. Fusion* **4** 131–8
[27] Ogasawara M *et al* 1980 *J. Phys. Soc. Japan* **49** 322–6
[28] Hirao A and Ogasawara M 1981 *J. Phys. Soc. Japan* **50** 668–72
[29] Bissell J J *et al* 2012 *Phys. Plasmas* **19** 052107
[30] Bissell J J *et al* 2010 *Phys. Rev. Lett.* **105** 175001
[31] Kho T H and Haines M G 1985 *Phys. Rev. Lett.* **55** 825–8
[32] Kruer W L 1988 *The Physics of Laser Plasma Interactions* (Reading, MA: Addison-Wesley)
[33] Nishiguchi A *et al* 1985 *Phys. Fluids* **28** 3683–90
[34] Haines M G 1986 *Can. J. Phys.* **64** 912–8
[35] Haines M G 1997 *Phys. Rev. Lett.* **78** 254–7
[36] Craxton R S and Haines M G 1975 *Phys. Rev. Lett.* **35** 1336–9
[37] Stamper J A 1991 *Laser Part. Beams* **9** 841–62

[38] Johnston T W 1960 *Phys Rev.* **120** 1103–11
[39] Shkarofsky I P *et al* 1966 *The Particle Kinetics of Plasmas* (Reading, MA: Addison-Wesley)
[40] Brunner S and Valeo E 2002 *Phys. Plasmas* **9** 923–36
[41] Rickard G J *et al* 1989 *Phys. Rev. Lett.* **62** 2687–90
[42] Grishkov V E and Uryupin S A 2011 *Phys. Lett.* A **375** 1990–3
[43] Rosen M D 1999 *Phys. Plasmas* **6** 1690–9
[44] Ridgers C P 2009 private communication
[45] MacDonald W M, Rosenbluth M N and Chuck W 1957 *Phys. Rev.* **107** 350